EXPERIMENTAL AND NUMERICAL INVESTIGATION OF OIL RECOVERY FROM BAKKEN BY MISCIBLE CO_2 INJECTION

A REPORT SUBMITTED TO THE DEPARTMENT OF ENERGY RESOURCES ENGINEERING

OF STANFORD UNIVERSITY

IN PARTIAL FULFILLMENT OF THE REQUIREMENTS FOR THE DEGREE OF MASTER OF SCIENCE

By
Ke Zhang
June 2016

I certify that I have read this report and that in my opinion it is fully adequate, in scope and in quality, as partial fulfillment of the degree of Master of Science in Petroleum Engineering.

Prof. Anthony R. Kovscek

(Principal Advisor)

Abstract

Unconventional liquid reservoirs are characterized by small matrix permeability that is several orders of magnitude lower than conventional oil reservoirs. The combination of multi-stage hydraulic fracturing and horizontal drilling has improved the overall profitability of these tight-oil reservoirs by enhancing the wellbore - matrix connectivity. Under primary production, however, the recovery factor remains in the range of only 5% to 10%. Considering such a large resource base, even small improvements in productivity could lead to billions of barrels of additional oil. Therefore, the need to develop a viable enhanced oil recovery technique for unconventional oil reservoirs is evident.

This study investigates technical feasibility of carbon dioxide as an enhanced oil recovery agent for tight-oil reservoirs. Above minimum miscibility pressure (MMP), CO_2 and oil are miscible leading to reduction in capillary forces and therefore high local displacement efficiency. The miscibility pressure of CO_2 is also significantly lower than the pressure required for other gases, which makes CO_2 miscible injection attainable under a broad spectrum of reservoir pressures.

The coreflood experiments recovered more than 70% of the original oil from a Bakken core sample with an average porosity of 7.5% and permeability of 1.8 µd. CT scans at dual energies were used as an additional tool to visualize fluid flow and distribution at core level. We discovered that the impact of CO_2 penetration is better captured at a lower energy level where the X-ray attenuation mechanism of photoelectric absorption becomes dominant. There is another interesting observation that is different from what we have anticipated: the change in CT number is greater during the earlier period of production than the later period. Possible explanations include **1)** miscibility may have not been fully achieved early on in the production, **2)** lighter hydrocarbon components are preferentially produced with CO_2, leaving behind heavier components with denser properties.

To decipher the oil recovery mechanisms in the coreflood experiment, a numerical compositional model was constructed to reproduce the laboratory results. Vaporization of light hydrocarbon components into CO_2 is shown as a major recovery mechanism. Other controlling factors include re-pressurization, oil swelling, viscosity and interfacial tension reduction. History matching with the laboratory experiment introduces additional complexities such as rock heterogeneities and presence of a fracture that promotes flow perpendicular to the core length. The above issues need to be addressed in order to match the displacement process exactly.

Acknowledgments

I've always been blessed in life to have great mentors. Their guidance and support are instrumental to my personal development.

My interest in the topic of petroleum dates back to college when I first interned with Schlumberger. Thanks to Dr. Mehmet Parlar and Joseph Ayoub who decided to hire me despite the fact that I had no work experiences in the oil & gas industry. They've shown unconditional support in my pursuit of learning and always encouraged me to step outside my comfort zone. If it weren't for them, I would not have had the courage to publish my first SPE journal paper and to give a technical presentation at an international symposium in front of a room of professional engineers.

Subsequently, I want to express my deep appreciation to Donald Lee and Dr. Najib Abusalbi, both with Schlumberger, Dr. Erik Haroz with Los Alamos National Laboratory and Rafael Cobenas with Chevron. They all made an investment in my professional and personal growth, for which I will always be grateful. I also want to thank Dr. Birol Dindoruk for providing constructive feedback on both my research and my future career choices, Phil MacNaughton and J.P. Chevriere for being like families while I am away from home.

I am most grateful to my advisor Dr. Anthony Kovscek who welcomed me into his research group. His advice has been instrumental to my research and I thank him for his patience and commitment to my personal advancement. I want to especially thank him for his support and encouragement during times of frustration and for giving me flexibility when conflict arises between research and coursework. I am fortunate to have had Dr. Kovscek as my advisor. He has played an important role in making my Stanford experience a positive one.

I want to thank the members of SUPRI-A team, especially Elliot Kim, Bolivia Vega, Hamza Aljamaan, Khalid Alnoaimi and Guenther Glatz for their assistance in the laboratory and feedback on my research. I am also grateful to ERE faculties and staffs for making my experience at Stanford memorable.

Finally, I'd like to thank my families who always love me and support me to pursue my dreams and ambitions. They made great sacrifices in their life so I can stand where I am today. I dedicate this thesis to my parents Hebo Zhang and Yaling Fan.

Contents

List of Tables

List of Figures

Chapter 1

1. Introduction

This thesis presents experimental and numerical modeling results from a miscible CO_2 flood aimed to assess enhanced oil recovery prospects in liquids-rich shale reservoirs, characterized by low matrix permeability and porosity. To produce from liquids-rich shale reservoirs efficiently, a thorough understanding of flow mechanisms, reservoir properties, rock and fluid interactions is necessary.

1.1. Background and Problem Statement

Production of light oil and gas condensates from shale oil reservoirs in North America is more economical than production of dry natural gas. Therefore, many companies have directed their efforts towards liquids production, as shown in Figure 1-1 (a). Eagle Ford and Bakken formations have contributed significantly to the overall U.S. domestic production. Figure 1-1 (b) shows that U.S. oil production increased from 5 million barrels/day in 2005 to 6.5 million barrels/day in 2012 reversing a decline trend that started in 1986 (EIA, 2013).

The hydrocarbons have been known to exist in the formations for decades, but their exploitation was not economic due to low matrix permeability, often on the order of micro to nano-darcy. Recent technological advances in multi-stage hydraulic fracturing and horizontal drilling that first enabled the exploitation of tight gas plays such as the Barnett Shale were later successfully implemented in tight-oil reservoirs. They have dramatically improved the overall profitability of tight-oil production by enhancing the matrix – wellbore connectivity. In spite of economic oil rates given by the combination of fracturing and horizontal drilling, significant capillary forces related to small pores and pore throat sizes cause the majority of oil to be trapped in the low permeability rock matrix. Typically, production declines rapidly and stabilizes at a low rate, ranging from 5% to 10% (Hoffman, 2012). With such low primary recovery factors, but a large resource base, even small improvements in productivity could lead to billions of barrels of incremental oil. This prospect makes the application of enhanced oil recovery a necessary step to exploit efficiently the unconventional oil reservoirs, and in the meantime, extend the life of assets.

Two issues pertaining to enhanced oil recovery prospects in liquids-rich shale reservoirs were addressed in this thesis. First, recovery potential of a miscible CO_2 flood was quantified through benchtop coreflood experiments. Due to low rock permeability and porosity, standard coreflood apparatus and equipment were modified accordingly. Second, a compositional flow simulation model was constructed to understand recovery mechanisms for tight-oil reservoirs.

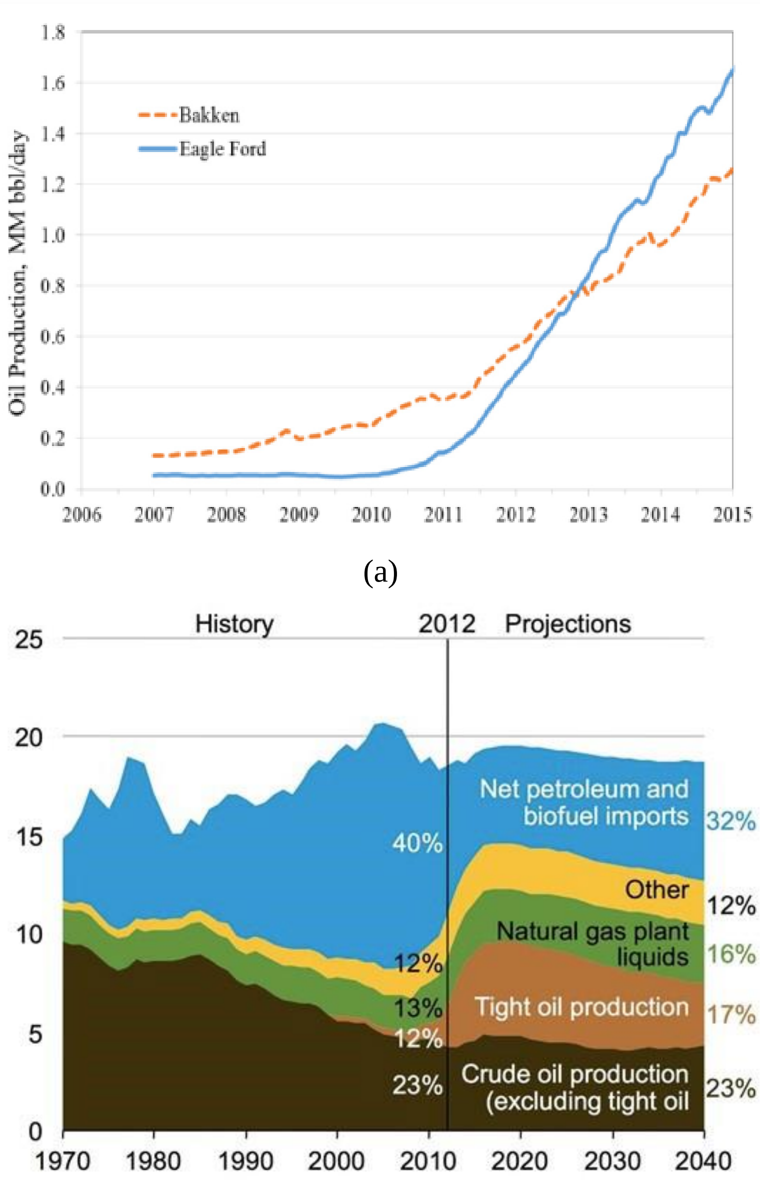

(a)

(b)

Figure 1-1: Significance of U.S. tight oil production (Energy Information Administration, 2013).

1.2. Objectives

There are three major objectives of this study. First, feasibility of CO_2 as an enhanced oil recovery agent is evaluated through coreflood experiments conducted at miscible conditions. Second, the use of X-ray computed tomography provides additional information on multi-phase flow and fluid distribution at the core scale. Last, a compositional model is built and optimized in an effort to reproduce experimental trends observed in the laboratory and to have a better understanding of the proper physics.

Chapter 2

2. Literature Review

In this chapter, a brief assessment of the Bakken formation is presented, including its geological structure, and most recent estimate of proven reserves and OOIP. Then, feasibility of CO_2 as a potential EOR agent for Bakken reservoirs is discussed. Both simulation and experimental results from previous research efforts show that CO_2 injection increases recovery and outperforms primary production. In the end, X-ray computed tomography (CT) is introduced as an efficient and accurate technique to visualize multiphase flow in a porous medium both qualitatively and quantitatively. Methods of computing porosity from CT images and potential sources of image artifacts are also described in detail.

2.1. Overview of Bakken Formation

The Bakken is in the Williston Basin that is a large sedimentary basin that covers parts of North Dakota, Montana, South Dakota, Saskatchewan, and Manitoba as shown in Figure 2-1. As one of the largest unconventional resources in the world and most prolific tight oil plays in North America, the Bakken petroleum system has approximately 7.4 billion barrels of technically recoverable oil as estimated by the U.S. Geological Survey in 2013 (Gaswirth et al., 2013) and original oil in place is considered to be up to 167 billion barrels (Nordeng et al., 2008).

The Bakken formation overlies the Upper Devonian Three Forks formation and underlies the Lower Mississippian Lodgepole formation as shown in Figure 2-2 (a). Stratigraphically, Bakken formation is comprised of three members: the Upper, Middle and Lower Bakken. The upper and lower members of the North Dakota Bakken formation consist of organic-rich shales with a total organic carbon (TOC) content ranging from 12 to 36 weight percent (Tran, 2011). Both of these shale members contain a high concentration of Type II kerogen and act as the source rocks for the petroleum in the Bakken formation. The middle member is organic-poor, with TOC content of 0.1 to 0.3 weight percent and is the main reservoir (Kurtoglu et al., 2013). While oil may be directly produced from its shales, the majority of Bakken wells have been drilled horizontally into the Middle Bakken where geology is most favorable in terms of having relatively larger porosity (5 – 8%) and permeability (less than 50 µd) (Theloy, 2014).

The Middle Bakken lithology varies from clastics (including silts and sandstone) to carbonates (silty dolomites), with six distinct lithofacies identified in Figure 2-2 (b) (Theloy, 2014). MB-C is of particular interest here due to distribution of highly laminated zones. The laminations in MB-C not only display slightly larger porosity but also are generally geo-mechanically weaker than other Bakken lithofacies and therefore more prone to fracturing during well stimulation processes (Kurtoglu et al., 2013).

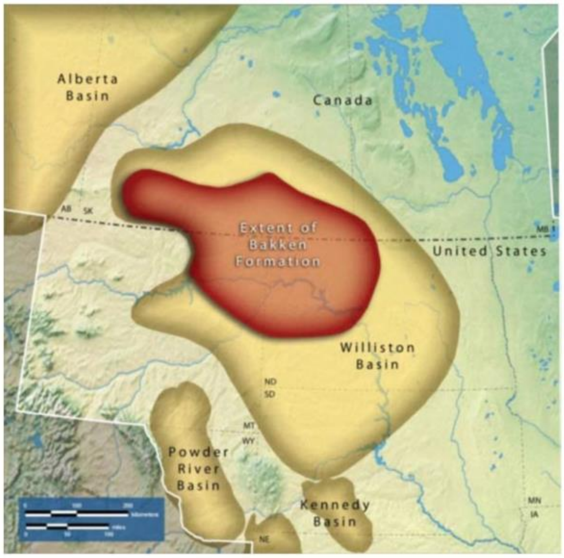

Figure 2-1: Bakken formation in Willison Basin (Sorensen et al., 2010).

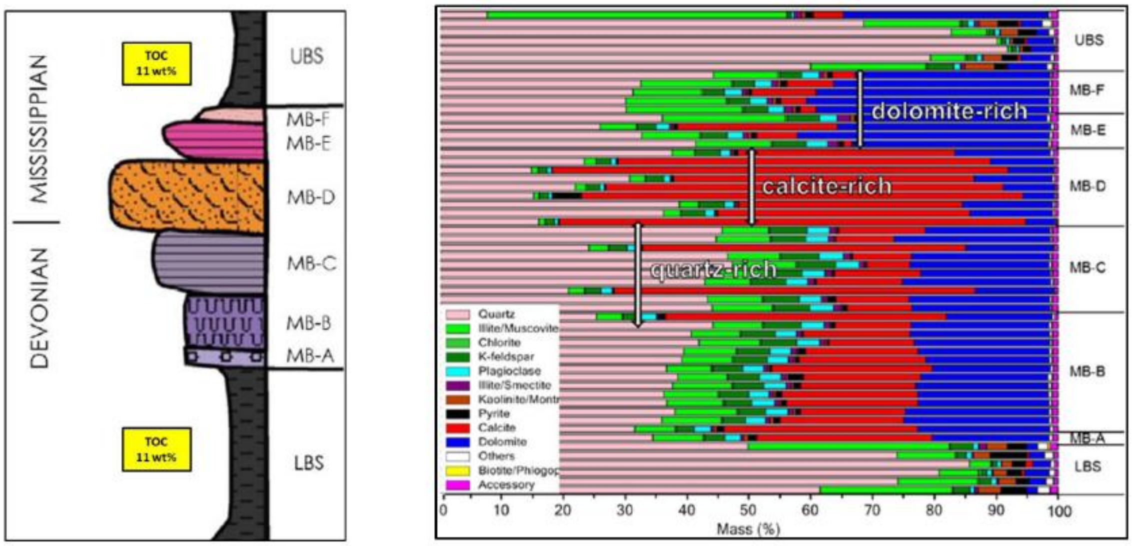

(a) (b)

Figure 2-2: (a) Stratigraphy chart of the Bakken Petroleum System, (b) Mineralogical composition of Middle Bakken facies and Bakken shales based on QEMSCAN data. LBS = Lower Bakken shale; MB-A through MB-F = Middle Bakken facies; UBS = Upper Bakken shale (Theloy, 2014).

The Bakken in the U.S. portion of the Williston Basin produces oil from numerous reservoirs such as the North Dakota Antelope field (1953), Montana Elm Coulee field (2000), and North Dakota Parshall and Sanish fields (2006). Elm Coulee is the most productive Bakken field producing mainly from the Middle Bakken member of Bakken Formation. Its discovery and successful development set the stage for further exploration leading to other discoveries in the

Williston Basin in 2006 to include Parshall, Sanish, Reunion Bay, Bailey, and Murphy Creek fields (Kurtoglu, 2013).

2.2. Discussion of Different EOR Options

The challenge with enhanced oil recovery in unconventional oil reservoirs such as Bakken is the difficulty to direct injected fluids through well perforations to hydraulic fractures, to natural or induced fractures and eventually deep into the pore space to displace oil from the low permeability rock matrix (Kurtoglu et al., 2013). Water flooding is common to conventional reservoirs, but does not appear as a viable secondary option here due to low injectivity and the oil-wet nature of the Bakken reservoirs. Wettability describes the preference of a solid to be in contact with one fluid rather than another. A strongly oil-wet surface prefers contact with oil. Therefore, under waterflood, a greater entry pressure is necessary to overcome the barrier of capillarity effect. Thermal recovery is generally used to produce viscous heavy oil. Oil viscosities in shale oil reservoirs are very low therefore the mechanism to reduce oil viscosity from thermal methods will not be significant. Figure 2-3 gives an overview of current range of reservoir depth and oil viscosities where main EOR technologies are applied (Poellitzer et al., 2009). Literature reviews show that a typical Bakken reservoir is at least 9000 feet deep, and produces a light crude oil with viscosity less than 1 cP at reservoir conditions. The combination of these two properties makes gas injection the most optimum choice for Bakken.

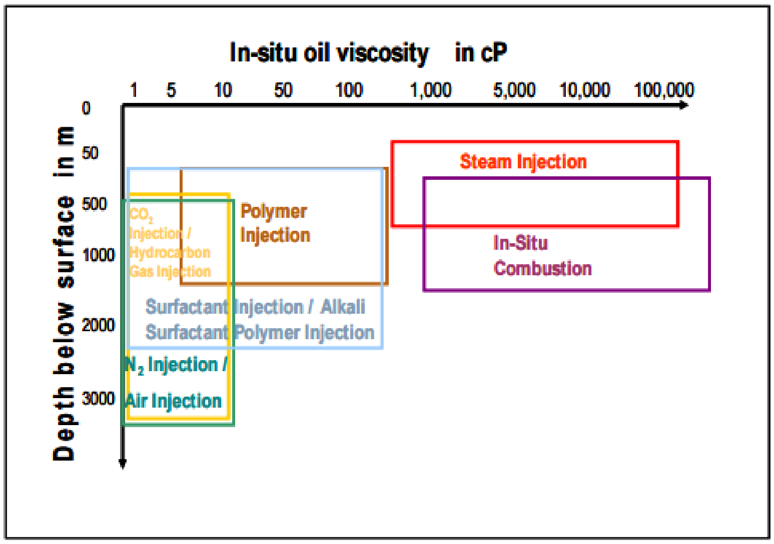

Figure 2-3: Screening of different EOR techniques based on reservoir depth and in-situ oil viscosity (Poellitzer et al., 2009).

Gas injection is the most widely applied EOR process for light to medium grade crude oils. We consider it as the most optimum EOR option for shale oil reservoirs. Oil recoveries from gas injection processes are usually the greatest when they are operated under conditions where gas becomes miscible with the reservoir oil. The primary objective is to improve local displacement efficiency and reduce residual oil saturation below the levels typically obtained by water flooding. Examples of miscible gas injectants are CO_2 or N_2 at sufficiently high pressure (MMP) and dry gas enriched with sufficient quantities of LPG components (MME). Usually, CO_2 displacements are more efficient than N_2 or CH_4 but any of the methods will work in deeper reservoirs and the final choice often depends on local availability and cost of the gas to be injected (Taber et al., 1997).

As a matter of fact, gas injection, in most general senses, is the method of choice for EOR processes. Rao (2001) argued that gas-based EOR method is “the solitary hope” for revitalization of mature reservoirs. There are well-accepted facts that waterflood recoveries from conventional reservoirs rarely exceed 40% of original oil in place (OOIP); that most waterfloods are maturing or close to their economic limits; and that chemically enhanced waterfloods appear to have become practically extinct due to cost effectiveness in spite of their conceptual soundness.

2.3. CO_2 EOR for Unconventional Liquids-Rich Reservoirs

We advocate CO_2 as the fluid of choice for EOR in the Bakken formation because of the following characteristics (Harju, 2012):

- CO_2 dissolves in oil easily, swells the oil, and lowers its viscosity, thereby allowing oil to flow more freely.

- CO_2 has a lower miscibility pressure with Bakken crude than other gasses such as nitrogen and hydrocarbon gases. CO_2 requires a minimum reservoir pressure of 1100 psi (North Dakota Bakken > 4000 psi) and temperature between 90°F to 250°F (North Dakota Bakken ranges from 150°F to 240°F). Above MMP, CO_2 has a zero pressure barrier to enter into oil-filled pore space and extracts the lighter components of oil from the matrix with significant efficiency.

- CO_2 EOR is the most effective when oil gravity is between 27 and 48 °API. Bakken produces a light crude from 36 to 48 °API.

- CO_2 injection re-pressurizes the reservoir, thereby re-establishing a drive mechanism.

- A portion of injected CO_2 is recycled at the surface.

- CO_2 injection can mitigate carbon emissions to the atmosphere by storing CO_2 in the reservoir. The shale organics are nano-porous materials characterized by large internal surface areas that can absorb significant amount of gases.

CO_2 injection has been widely used in conventional reservoirs and reported to be successful during field applications even under unfavorable conditions such as heavy oil and naturally fractured reservoirs where water flooding is no longer effective (Beliveau, 1987; Sahin, 2008). By 2012 CO_2 miscible flooding accounted for 308,564 barrels/day of oil, 41% of the total U.S. EOR daily production, which is more than any other EOR methods. CO_2 immiscible added another 43,657 barrels/day (Anonymous, 2012).

While the effectiveness of CO_2 injection in conventional reservoirs is well understood, its use for EOR in tight-oil reservoirs is still a new concept that attracts numerous interests from the oil industry and academia. Below is a brief overview of established work that aims to evaluate the viability of CO_2 as an enhanced oil recovery agent for tight oil reservoirs. Both experimental and simulation results show encouraging increases in recovery as a result of CO_2 injection.

Shoaib and Hoffman (2009) used a numerical flow simulator to model a sector of the Elm Coulee field with a low permeability in the range of 0.01 to 0.04 md and a homogeneous porosity of 7.5% from log analyses. Two different reservoir models were built: a primary recovery and a CO_2 flood model. They were used to determine the additional recovery by CO_2 injection. The CO_2 flood model was further executed with different scenarios to determine the best well locations and injection schemes for maximum sweep efficiency from CO_2 flooding. The scenarios included comparison between horizontal and vertical injection, continuous CO_2 injection and cyclic CO_2 treatment, different well patterns and the amount of CO_2 injected. The optimum well development and injection strategy obtained from the above study was then incorporated by Hoffman (2012) into his subsequent work that led to the conclusion that miscible CO_2 injection increases recovery from 6.02% under primary production to 21.58% of OOIP.

Mohanty et al. (2013) investigated miscible CO_2 huff and puff in a shale matrix representative of the Bakken formation. A simulator was used to include multiple vertical fractures along a horizontal well in a formation with permeability and porosity of 0.01 md and 8%, respectively. CO_2 injection was found to outperform primary production for a heterogeneous reservoir.

Liu et al. (2014) constructed a fine-scale model with a pair of horizontal wells to examine the effectiveness of CO_2-based oil recovery techniques. Results indicated that production could be enhanced by 43% to 58%, and incremental recovery was very sensitive to the relative permeability curves used in the simulation. The authors of this paper believe that their CO_2 flooding results in increased production because the permeabilities of their model are on the order of milli-darcy in the well areas and in the order of tens of milli-darcy in some simulation cells. Such high permeability in the well-connected area is similar to a conventional reservoir.

Vega et al. (2010) studied miscible CO_2 injection into siliceous shale of 1.3 md permeability and 34% porosity. Experimental results, aided by X-ray computed tomography image analysis demonstrated that CO_2 was able to penetrate from the fracture to the matrix and recover up to 93% of OOIP. In addition, pyrochromotographic analysis of the collected oil sample revealed the compositional changes with respect to the original oil. The trend of extraction of relatively light components was seen throughout the counter-current and co-current cycles.

Tovar et al. (2014) presented their experimental results on the use of CO_2 as an EOR agent in preserved, rotary sidewall reservoir core sample with permeability in the nano-darcy range. Core samples were packed into a core holder using glass beads to simulate the presence of a conductive hydraulic fracture. The core was soaked in CO_2 for several days before production was allowed in intervals. The operating temperature was 150°F and two pressures were used in the experiments: 3000 psi and 1600 psi. Fluid saturations were visualized using X-ray computed tomography and qualitative comparisons were made with the length of soaking time.

Tovar et al.'s (2014) experiments faced a series of challenges. For example, the petrophysical properties of the cores (e.g. porosity and permeability) were unknown because the core had such low permeability that volumetric methods to calculate pore volume were dismissed. In the absence of information on porosity, they decided to estimate the performance of CO_2 EOR by proposing a number of scenarios with porosity given in the range of 0.3% to 0.6% and initial water saturation from 0 to 30%. Following this methodology, oil recovery was estimated to be between 18% and 55% of OOIP. The low volume of oil recovered prevented them from measuring API gravity, viscosity or oil composition. From visual inspection, however, oil collected from their experiments had a lighter color and lower viscosity compared to oil produced from the field. This observation supports Vega et al.'s conclusion that vaporization of hydrocarbons into CO_2 is a main recovery mechanism.

Alharthy et al. (2015) presented both laboratory and numerical modelling of EOR in Bakken cores using CO_2, C_1-C_2 mixture and N_2. Porosity is in the range of 4.5 – 8.1%, and permeability is in the range of 0.002 – 0.04 md. CO_2 was injected at a constant pressure of 5000 psi while temperature is maintained at 230°F. The core was soaked in CO_2 for 50 minutes before a production interval of 10 minutes. There was space between the inside of the extraction vessel wall and the cylindrical core which simulated the presence of a fracture surrounding the core matrix. This allowed CO_2 to flush around the core sample as opposed to being forced through. The experiments recovered more than 90% oil from several Middle Bakken cores and nearly 40% from Lower Bakken cores. A numerical compositional model was then constructed to match laboratory oil recovery results and understand the mass transfer mechanisms for liquid-rich shales.

Alharthy et al. (2015) concluded that the main recovery mechanism was miscible oil extraction at the matrix-fracture interface. This promoted counter-current flow of oil from the matrix instead of oil displacement through the matrix, which was normally seen in conventional, more permeable reservoirs. Other controlling factors included oil swelling, viscosity and interfacial tension reduction, wettability alteration and etc. From the history matching of solvent soaking EOR processes, they made the observation that the synergy of fluxes (diffusive-advective mass transfer) was critical in order to mimic the proper extraction physics.

2.4. Tomographic Imaging of Multiphase Flow in Porous Media

The use of X-ray computed tomography (CT) for visualizing single and multiphase fluid flow in rock and other porous media is a relatively new technique in petroleum engineering and geosciences. When a CT scanner is operated, X-rays penetrate a thin volumetric slice of an object at angular increments within a single plane. A series of detectors then record the transmitted X-ray intensity. Back projection algorithms using Fourier transformation are then employed to reconstruct a cross-sectional image based on measurements of different X-ray attenuations (Akin & Kovscek, 2003).

After image reconstruction, the computer converts attenuation coefficients into corresponding CT numbers by normalizing with linear attenuation coefficient of water, μ_w

$$CT = 1000 \frac{\mu - \mu_W}{\mu_W} \tag{2-1}$$

The linear attenuation coefficient is a function of both electron density, ρ and effective atomic number, Z in the following form (Vinegar & Wellington, 1987):

$$\mu = \rho(a + b\frac{Z^{3.8}}{E^{3.2}}) \tag{2-2}$$

Where *a* is the Klein-Nishina coefficient and *b* is a constant. For X-ray energies above 100 keV, X-rays interact with the matter by Compton scattering that depends on electron density. For energies well below 100 keV, the interaction is dominated by photoelectric absorption that depends on the effective atomic number.

There are several challenges in imaging miscible coreflood experiments with shale. First, oil and CO_2 have very similar densities at miscible conditions. This facts makes it difficult to track either component in the fluid mixture. Second, a low porosity may lead to high noise-to-signal ratios from the CT scans. These issues will be addressed in more detail later on.

2.4.1. Determination of Porosity

Withjack (1988) performed CT porosity measurements from two well-aligned images of a porous medium saturated with different fluids. The following equation, based on Beer's law, is applied to determine porosity from each voxel:

$$\phi = \frac{CT_{or} - CT_{ar}}{CT_{oil} - CT_{air}} \tag{2-3}$$

The subscripts *or* and *ar* represent oil- and air/vacuum-saturated rock respectively. A close agreement of +/-1% was reported between the CT-derived porosities and those determined from the conventional volumetric methods.

2.4.2. Image Artifacts

Measurements with X-ray CT are subject to a variety of errors including beam hardening, X-artifacts and positioning errors. Because an X-ray source delivers a spectrum of X-ray energies, the lower energy or soft portions of the X-ray spectrum are absorbed preferentially by the sample itself. This introduces an error in linear attenuation measurements because the remaining high-energy photons shift the average energy of the spectrum toward harder X-rays. This results in falsely high CT numbers and manifests as a dark band around the periphery of objects. There are several ways to reduce or even eliminate beam hardening effects. For example, in a third generation CT scanner, detectors are collimated to reduce object scattering. Aluminum and composite carbon fiber core holders are fabricated for such purposes as well. Beam hardening effects are also reduced by simply moving to higher energy X-ray sources with fewer low energy photons.

Object shape also leads to potential image artifacts. Because the geometry of the scanner gantry is circular, X-shaped artifacts are observed when square or rectangular cross-sectional objects are presented to the scanner. This type of artifact originates from the image reconstruction process by assuming that an average attenuation can be applied along each ray path. In square or rectangular shaped images, the length of diagonals is greater than the side lengths. Therefore, CT numbers are largest there even for homogeneous materials.

Lastly, positioning errors can be introduced during the process of image subtraction to obtain porosity and in-situ saturation measurements. The objects being scanned must either remain stationary or be fixed to a positioning system for repeatable return to exactly the same position.

Chapter 3

3. Coreflood Experiments and Methodology

In this chapter, petrophysical properties related to the Bakken core sample are presented in addition to a detailed description of experimental set-up and procedures.

3.1. Bakken Core Description

The core sample used in the experiment was obtained at a depth of 11,340.07 feet from the North Dakota Bakken formation. It is 1 inch in diameter and 2 inches in length. The absolute permeability (to oil) is 1.8 µd and the average porosity is 7.5%. Figure 3-1 gives a visual description of the core sample in addition to a three-dimensional porosity distribution obtained from CT image analysis. The core matrix is considered mostly homogeneous with some localized heterogeneities that we identify as laminations parallel to the core face.

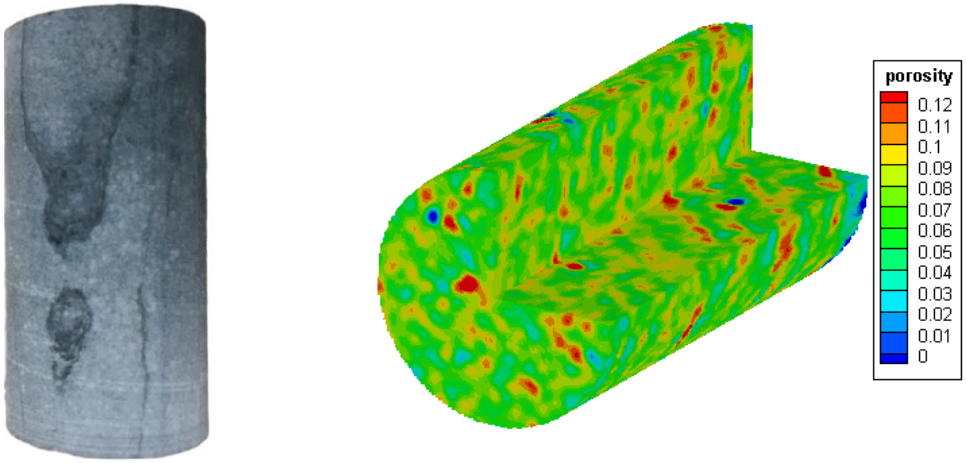

(a) (b)

Figure 3-1: The Bakken shale core sample. (a) Wax-preserved core plug, (b) 3-D volume reconstruction of CT-derived core porosity.

3.2. Determination of Miscibility Pressure and Temperature

Miscibility experiments were performed using a CT scanner and a vanishing oil-gas phase boundary technique on the Bakken fluid sample. An aluminum sleeve was charged with dead Bakken crude and CO_2 and scanned at different pressures and a fixed temperature at 38°C. Disappearance of two phases and formation of a single phase is indicative of miscibility. In theory, miscibility pressure increases with increasing temperature. Because the coreholder had a pressure rating of only 2000 psi, the test temperature was lowered to 38°C (slightly above critical temperature of CO_2) in order to achieve miscibility at pressures attainable within the experimental apparatus. Figures 3-2 (a) to (d) demonstrate changes in fluid behavior between oil and CO_2 at an increasing pressure inside the aluminum tube. Magnitude of CT number is indicative of fluid density. A denser fluid has a greater CT number. At ambient pressure, there is a distinct interface between oil and CO_2 due to a large difference in phase densities. As pressure increases, more CO_2 dissolves in oil and the oil phase starts to swell. At a pressure of 1200 psi and beyond, the phase boundary completely disappears and the fluid mixture becomes a single phase as shown in Figure 3-2 (d).

Using this method, we determine a miscibility pressure of 1200 psi at the chosen temperature. We understand that a typical Bakken reservoir has a much greater temperature (150 - 240°F) than 38°C. Reservoir pressure (>4000 psi) is also significantly greater than what has been predicted here so miscibility can still be achieved. Due to experimental limitations, we cannot reproduce the actual reservoir conditions; however, the purpose of this study is to better understand the recovery mechanism of miscible CO_2 displacement and its feasibility for a tight-oil reservoir.

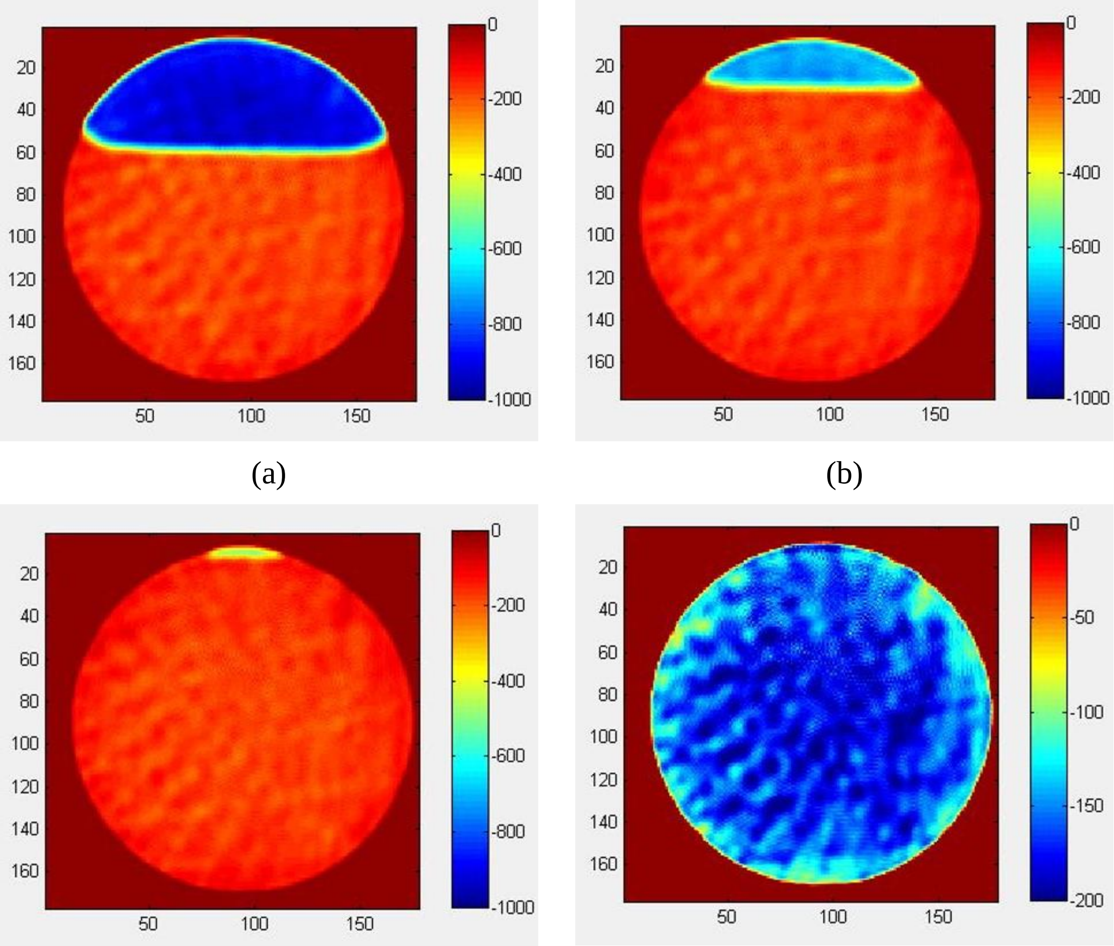

(a) (b)

(c) (d)

Figure 3-2: CT scans of CO_2 and Bakken crude in an aluminum tube at 38°C and varying pressures at 0.625 mm spacing, 140 keV/120 mA. (a) Ambient pressure, (b) 1000 psi, (c) 1100 psi, (d) 1200 psi.

3.3. Experimental Setup

Because the core sample is low permeability and low porosity, standard coreflood apparatus and equipment is modified accordingly. As shown in Figure 3-3, the coreholder is wrapped with electrical heating tape and connected to a temperature controller to maintain a constant temperature at 38°C. CO_2 is pressurized in a stainless steel gas accumulator and an ISCO pump is used to inject CO_2 at 1500 psi at the inlet valve of the core holder. Confining stress is set to at least 500 psi above the pore pressure and the downstream pressure is maintained through a back pressure regulator (BPR) at 1300 psi. Oil effluent exits the BPR and enters a long coiled tubing immersed in cold water inside an Erlenmeyer flask. The coiled tubing is designed to function as a condensing unit to capture any light-oil components that may have vaporized into the gas phase. The volume of oil recovered is measured indirectly via a mass scale with a minimum reading of 0.01 g. A constant oil density of 0.8156 g/mL is used to convert mass back to volume, which has an equivalent accuracy of 0.01 mL. In addition, any gas production is captured in a separate apparatus using an inverted graduated cylinder pre-filled with water.

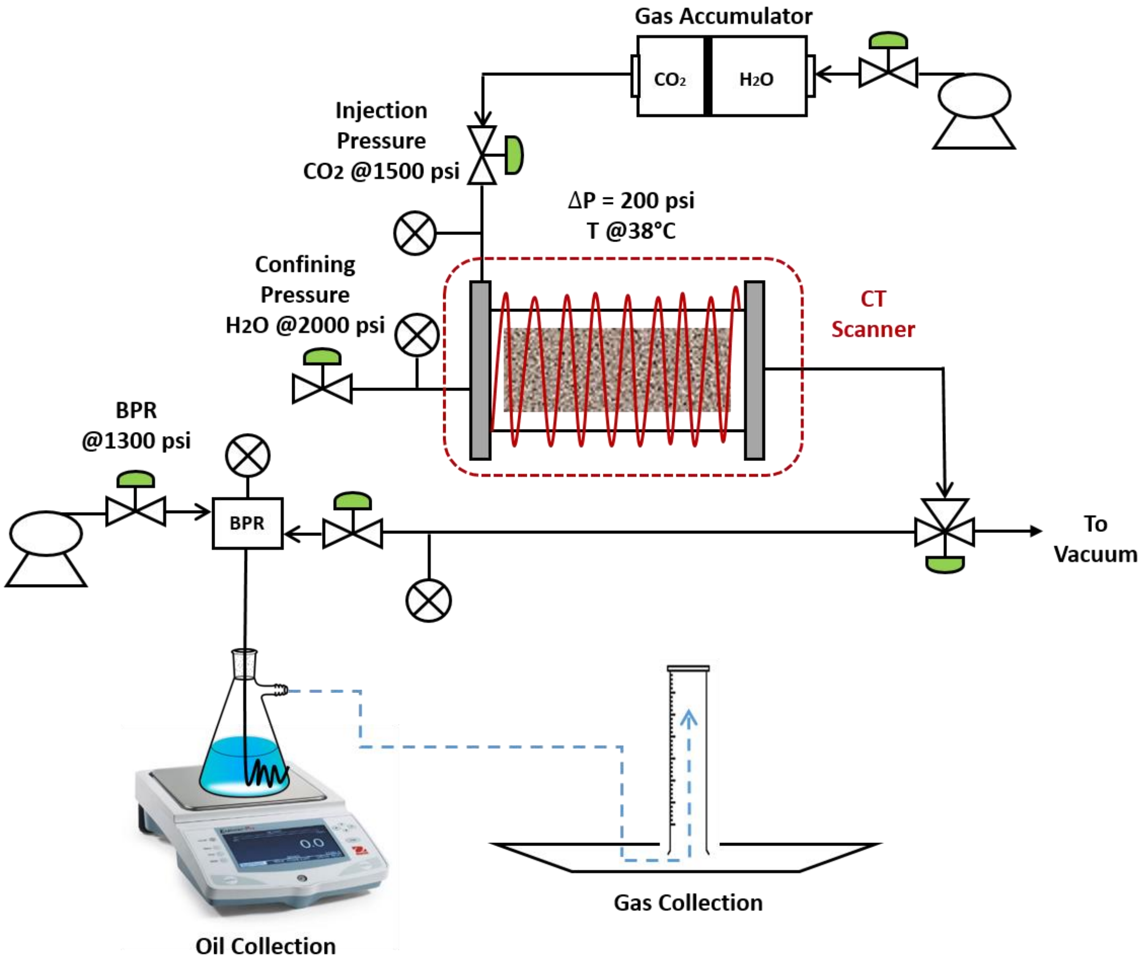

Figure 3-3: Schematic of experimental apparatus and equipment for coreflood experiment.

3.4. Experimental Procedures

The following section explains key steps relevant to experimental design of a miscible CO_2 flood.

3.4.1. Core Sample Preparation

The core sample is placed between two stainless steel end caps that provide access to a confining pressure system and to a pore pressure system. The sample is coated with a high temperature silicone gel (730 Solvent Resistant Sealant, Dow Corning) and sleeved with multiple layers of heat-shrinkable Teflon (PTFE HS 2:1 Heat Shrink, Zeus) and an additional layer of aluminum foil to prevent potential CO_2 diffusion into the confining space. The silicone gel requires at least 24 hours to cure and 3 to 5 days to provide maximum seal. The composite core sleeve isolates the core sample from the confining fluid (e.g. water) and allows realistic confining stress to be applied. An outer 1/6” thick aluminum sleeve slides over the core and seals via Viton O-rings at the end caps. Three threaded aluminum rods pass through the end caps to hold the entire apparatus together when subjected to high pressure. The apparatus is able to withstand a maximum pressure of up to 2000 psi. The design of the core holder is to ensure X-ray compatibility and try to reduce the effect of beam hardening during CT scanning.

3.4.2. Miscible CO_2 Flood

Figure 3-4 explains several key steps for the experiment of miscible CO_2 injection. The core sample is first saturated with decane and dried under vacuum for at least three days at an elevated temperature of 65°C to evaporate any residual decane in the pore space. Next, the core is fully saturated with dead Bakken crude oil. We assume no initial water saturation here. The oil-saturated core is then brought to a pressure and temperature of 1300 psi and 38°C. Note that this is well above the miscibility pressure specified earlier. CO_2 is injected at a constant pressure differential of 200 psi across the core with the downstream open for production.

The experiment is monitored under a CT scanner from initial oil saturation to subsequent injection of CO_2. Both oil images and CO_2 images at different pore volume injected (PVI) are obtained to better understand the recovery mechanisms of miscible CO_2 flood. The CT scanner used in this experiment is a GE Lightspeed Ultra Advantage third generation 8-slice scanner, featuring a 53 kW generator, 6.3 MHU tube and a fast gantry rotation time of 0.5 seconds. It has 16 parallel rows of solid-state detectors, covering 20 mm in the z direction at the iso-center (MHRA Evaluation Report, 2003). The voxel dimension is 0.19 by 0.19 by 1 mm, the tube current is 120 mA and X-ray energies of both 140 and 80keV are used sequentially. The X-ray exposure for one image is 1 second. The images obtained are flat and do not exhibit beam hardening effect largely due to the elevated energy level.

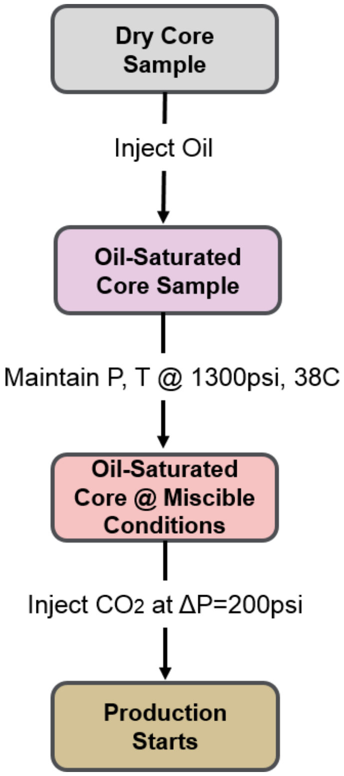

Figure 3-4: Proposed experimental sequence for miscible CO_2 coreflood experiment.

Chapter 4

4. Experimental Results

In this chapter, results from the coreflood experiment are presented and discussed in detail. This includes hydrocarbon recovery potential of a miscible CO_2 flood, as well as image analysis of dual-energy CT scans to visualize temporal development of fluid distribution at the core scale.

4.1. Hydrocarbon Recovery Potential

Figure 4-1 reports the recovery potential of miscible CO_2 flood for a Bakken core sample. A continuous CO_2 drive is simulated here instead of a “huff n’ puff” process. This experiment unfortunately stopped due to power outage midway during recovery. From the trend of existing data, we conclude that miscible CO_2 flood is able to effectively recover at least 70% of OOIP despite a small pressure gradient used in the experiment. It is also interesting to observe that almost six pore volumes of CO_2 are injected to recover 70% of the original oil. This suggests a potential reduction in local sweep efficiency due to matrix heterogeneities and low-permeability nature of the core sample. It is worth mentioning here that displacement of live oil should be more efficient than dead oil since there are more volatile hydrocarbon components to be extracted into the fast-flowing vapor phase and miscibility with CO_2 are more easily developed.

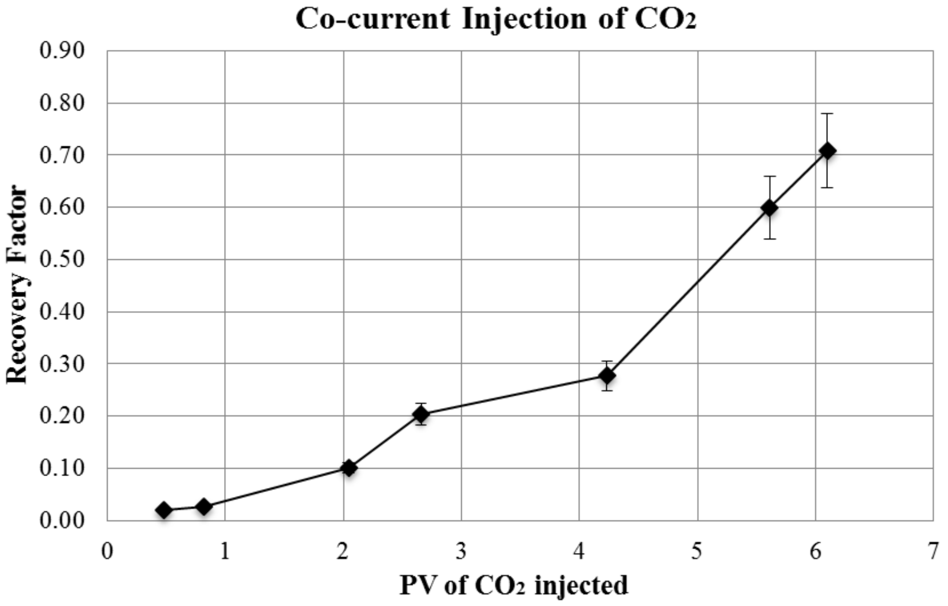

Figure 4-1: Hydrocarbon recovery from Bakken core with CO_2 solvent

4.2. CT Image Processing

CT images taken at different pore volumes of CO_2 injected are available to visualize temporal development of fluid flow and distribution at the core level. A dual-energy scan at 140 keV and 80 keV is used here to exploit the attenuation of X-rays by Compton scattering and photoelectric absorption. At 140 keV, interaction of X-ray with matter is dominated by Compton scattering that heavily depends on electron density. The density differences between oil and CO_2 at miscible condition makes it difficult to tell apart the two components from the CT scans. Therefore, we expect that the photoelectric effect from a lower energy level of 80 keV delivers a greater contrast. A number of different analyses have been done with the CT images. Important observations are presented below with possible explanations to some of the phenomena captured. The remaining study is included in Appendix B for brevity.

Figure 4-2 to 4-3 present 3-D reconstruction of a difference map of CT number at both energy levels for two different recovery factors. Note that all color legends have the same scale from 0 to -100 to be comparable. Because CO_2 has a lower pure fluid CT number than oil, the CT number of CO_2 images is expected to be lower than oil images. This translates into negative CT number differences when oil images are subtracted from CO_2 images to remove the contribution of rock matrix. A few observations are made as follows:

A comparison of Figure 4-2 and 4-3 confirms that impact of CO_2 penetration in the core matrix can be better captured at a smaller energy level than a greater energy level. This is demonstrated from the prevalence and also magnitude of negative CT number differences at 80 keV in Figure 4-3 for both recovery factors.

Suppose we can trace the footprints of CO_2 by locating all the negative CT number differences, it is observed that at an early recovery period, CO_2 preferentially accumulates at the top layer and the fracture region parallel to the core face. With progression of time and more oil recovered, CO_2 starts to populate the bottom layer as shown in both Figure 4-2 (b) and Figure 4-3 (b).

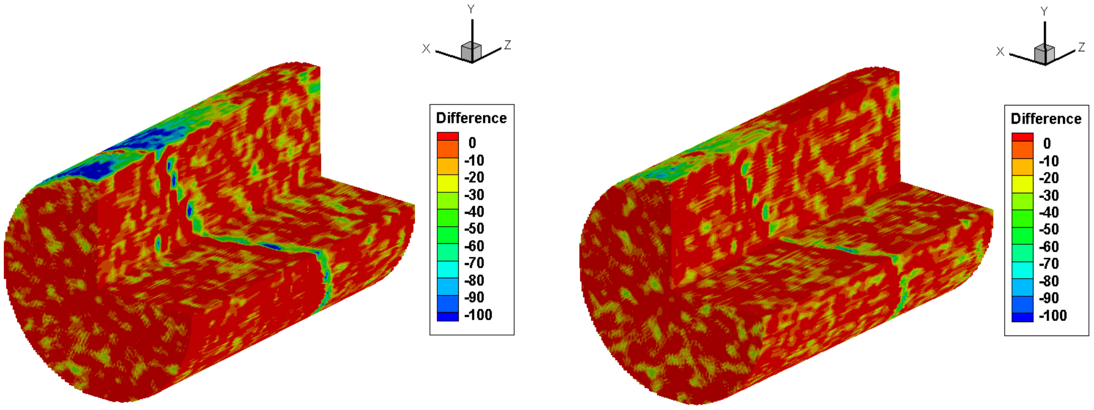

(a) (b)

Figure 4-2: Difference of CT number when oil images are subtracted from CO_2 images at a high energy level of 140 keV. (a) R_f = 20%, (b) R_f = 71%.

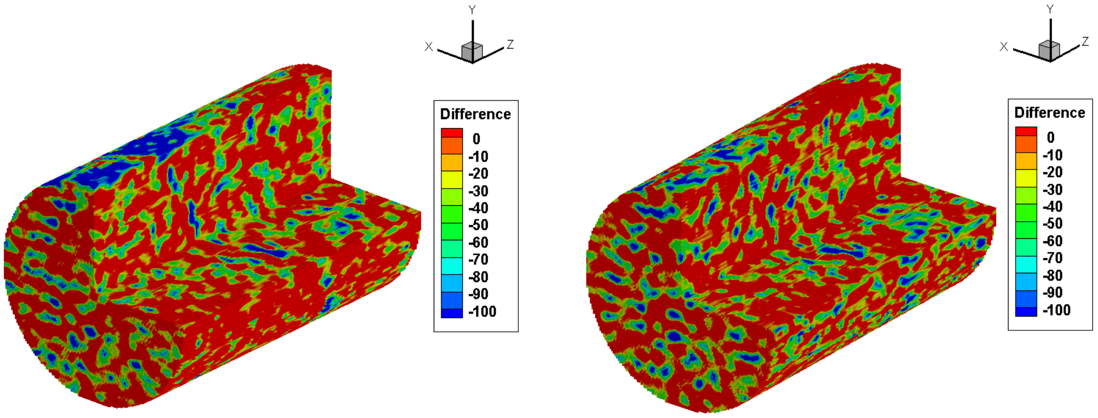

(a) (b)

Figure 4-3: Difference of CT number when oil images are subtracted from CO_2 images at a low energy level of 80 keV. (a) R_f = 20%, (b) R_f = 71%.

Chapter 5

5. Numerical Modeling of Laboratory Experiments

The following chapter presents numerical modeling of miscible CO_2 flood experiments with a Bakken core. First, gridding of the numerical model is presented. Then, a compositional model is built for a Bakken fluid sample and optimized with available PVT test results and experimental measurement of miscibility pressure. This serves as an essential input into subsequent flow simulation using Computer Modelling Group's (CMG) software packages.

5.1. Grid System

A single porosity-permeability Cartesian model was developed to test basic concepts before a more complicated model is incorporated. The cylindrical core is 1 inch in diameter and 2 inches in length. Properties (e.g. porosity and permeability) of certain grid blocks in the Cartesian model are modified to recover cylindrical geometry of the core sample. Specifically, as shown in Figure 5-1, cylindrical core matrix has a constant porosity of 7.5% whereas any other grid blocks outside the cylindrical boundary are assigned a porosity of 0 so they do not contribute to any fluid flow and storage. To mimic the actual experiment, an injector and a producer are added to the two ends of the core matrix with all grid blocks perforated and open to flow.

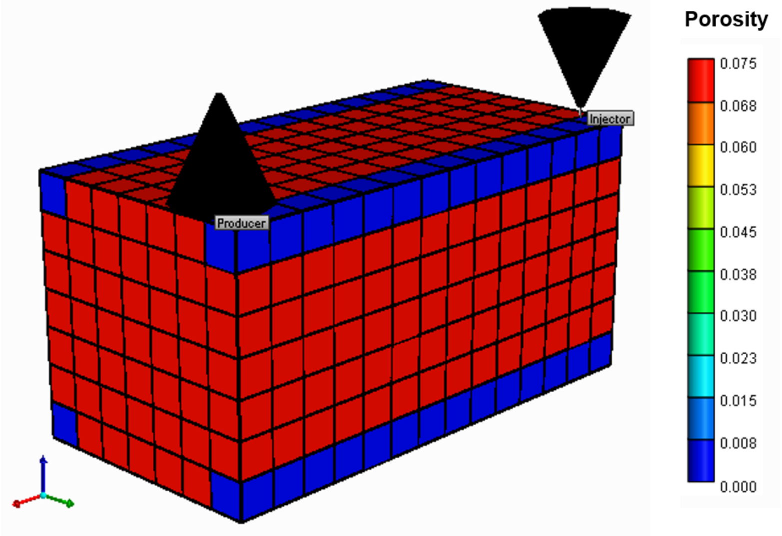

Figure 5-1: Single-porosity Cartesian grid (14 x 7 x 7) used in numerical modeling of miscible CO_2 flood experiment.

Table 5-1 shows matrix core properties. The core is treated as a homogeneous medium with constant porosity at 7.5% and permeability at 1.8 µd. For this base case, a coarse model (14 x 7 x 7) was used due to limitation on computing capabilities. We found that simulation run time increased significantly when more grid blocks were added. The effect of grid refinement was studied using a simplified 1-D model and results are summarized in Appendix C.

Table 5-1: Reservoir dimensions and properties for a laboratory model.

N_i, N_j, N_k (Cartesian Grid)	14 x 7 x 7
Core Length (inch)	2
Core Diameter (inch)	1
Matrix Porosity	7.5%
Matrix Permeability (μd)	1.8

5.2. Fluid System

Flow simulations are performed using CMG's GEM. A good compositional analysis of the Bakken crude is a necessary input into the flow simulator and is introduced using CMG's WinProp phase behavior and fluid properties tool. The use of a compositional simulator allows the definition of pseudo-ternary diagrams that facilitate the interpretation of the miscible processes.

It is practically impossible to describe all chemical components in a mixture of petroleum hydrocarbons, especially for the heavier fractions. Therefore a process referred to as lumping is used to represent a complex reservoir fluid with a manageable number of pseudo-components. In the subsequent compositional analysis, non-hydrocarbon gases (e.g. N_2 and CO_2) and light to medium hydrocarbons (C_1 – C_6) are considered defined components whose critical properties are widely available in the literature with great accuracy; heavier alkanes (C_{7+}), cycloalkanes and aromatics are lumped together and have density and molecular weight measured for the entire fraction.

The procedure of Pedersen et al. (1992) is used to first expand the plus fraction (C_{7+}) to 200 components and to re-group to 5 components. Here, intermediate fractions are characterized fairly well for the advantage of describing a miscible gas injection process. CO_2 remains as a distinct component because it is considered important in the final MMP calculation. In addition, nonzero binary interaction parameters are incorporated among **1)** methane and heavier hydrocarbon components and **2)** non-hydrocarbon gases (e.g. N_2 and CO_2) and heavier hydrocarbon components. All other hydrocarbon to hydrocarbon interactions are set to zero. The Peng-Robinson EOS with volume corrections is used throughout the analysis.

The properties of the heaviest fraction are used as tuning parameters to match the experimentally determined saturation pressure, oil density, oil viscosity and other properties from available PVT laboratory tests. The Modified Pedersen Corresponding States model (1987) is selected to predict liquid viscosity. This method gives better viscosity estimates than Jossi-Stiel-Thodos (JST) correlation for light to medium grade oil. Results of the regression study are summarized below.

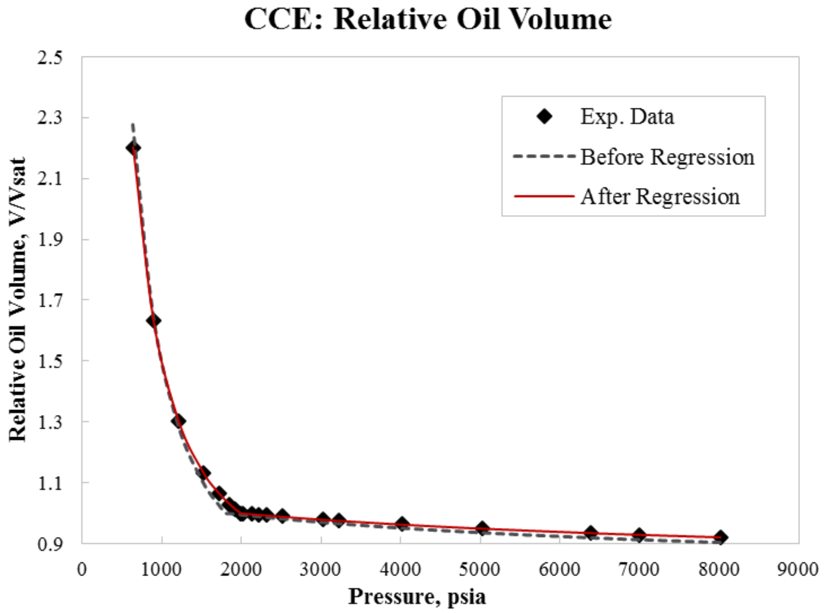
CCE: Relative Oil Volume
Relative Oil Volume, V/Vsat
Pressure, psia
2.5
2.3
2.1
1.9
1.7
1.5
1.3
1.1
0.9
0
1000
2000
3000
4000
5000
6000
7000
8000
9000
Exp. Data
Before Regression
After Regression

(a)

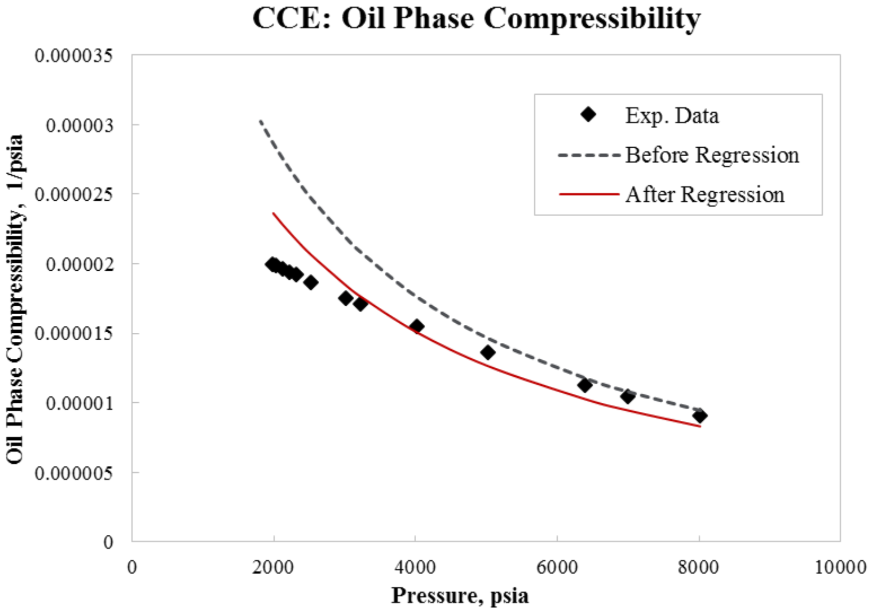
CCE: Oil Phase Compressibility
Oil Phase Compressibility, 1/psia
Pressure, psia
0.000035
0.00003
0.000025
0.00002
0.000015
0.00001
0.000005
0
0
2000
4000
6000
8000
10000
Exp. Data
Before Regression
After Regression

(b)

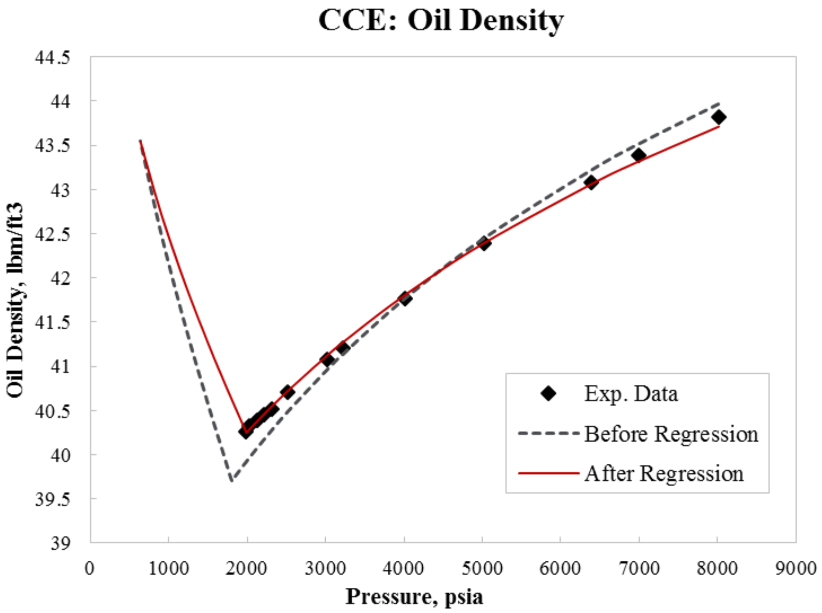

(c)

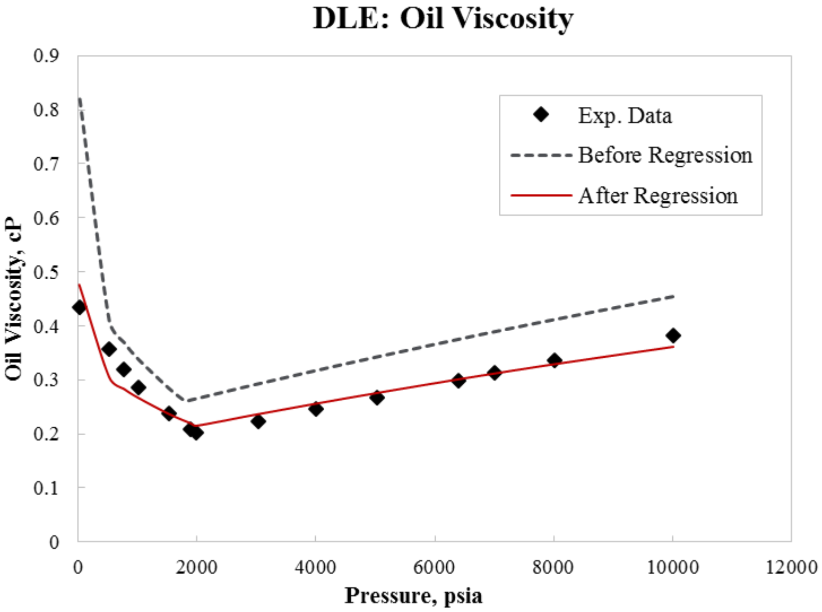

(d)

Figure 5-2: Comparison between EOS predictions and PVT data from Constant Composition (CCE) and Differential Liberation (DLE) experiments conducted at 237°F. (a) Relative oil volume, (b) Oil phase compressibility, (c) Oil density, (d) Oil viscosity.

Table 5-2 shows that a close match to experimental saturation pressure is achieved with an error of less than 0.3%. Figure 5-2 (a) to (d) summarize the comparison between lab data and model predictions for both CCE and DLE conducted at 237ºF. There is an almost perfect agreement with the simulated properties except for oil phase compressibility in Figure 5-2 (b). It appears that the simulated result matches more closely with the experimental data in the high-pressure range than the low-pressure range. We argue that both are in the same order of magnitude and therefore within the range of reasonable accuracy. Moreover, we do not anticipate large changes in pressure as the recovery process is not pressure depletion.

Table 5-2: Regression study for bubble-point pressure.

	Model Prediction	**Experimental Data**
Saturation Pressure (psia)	1991.51	1986

Figure 5-3 is a PT diagram constructed from the optimized EOS model that has shown to be capable of reproducing the phase behavior of Bakken reservoir fluid. The bubble point pressure is labelled as a red triangle. Table 5-3 summarizes the final pseudo-component description and input for EOS calculations. Note that the fluid model created for live oil (2nd column) is then used in a two-phase flash calculation to obtain molar compositions of dead oil (3rd column) deprived of light, volatile hydrocarbon components. This dead oil is considered more representative of the fluid sample used for our miscible CO_2 experiment and its composition is used as the initial input for the subsequent flow simulations.

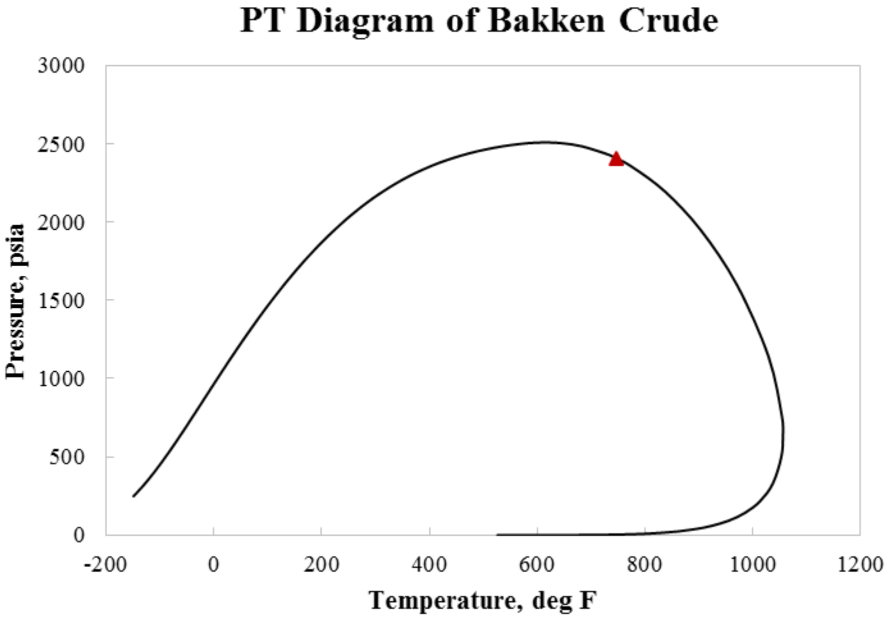

Figure 5-3: PT diagram from optimized EOS model representative of Bakken crude phase behavior.

Table 5-3: EOS parameters for optimized compositional model lumped into 12 components.

Component	Molar Composition of Live Oil	Molar Composition of Flashed Liquids	Pc (atm)	Tc (K)	Acentric Factor	MW (g/mol)	Volume Shift
CO_2	0.00260	0.00007	72.80	304.20	0.2250	44.01	-0.0817
N_2-CH_4	0.25056	0.00196	44.89	187.59	0.0094	16.58	-0.1609
C_2H_6	0.11868	0.00846	48.20	305.40	0.0980	30.07	-0.1134
C_3H_8	0.09758	0.02461	41.90	369.80	0.1520	44.10	-0.0863
IC_4-NC_4	0.06399	0.04314	37.17	421.49	0.1894	58.12	-0.0711
IC_5-NC_5	0.04029	0.05275	33.34	466.18	0.2421	72.15	-0.0470
C_6	0.03379	0.05922	32.46	507.50	0.2750	86.00	-0.0592
C_7-C_{10}	0.18346	0.37769	25.15	627.21	0.3205	137.76	0.0037
C_{11}-C_{13}	0.07872	0.16270	20.22	684.14	0.4595	198.20	0.0522
C_{14}-C_{17}	0.06091	0.12592	17.15	733.42	0.5751	255.58	0.0752
C_{18}-C_{21}	0.03244	0.06706	15.74	791.36	0.7013	322.90	0.0998
C_{22+}	0.03696	0.07641	10.57	1066.91	1.1184	344.97	0.0868

A multi-contact miscibility pressure of dead oil with CO_2 is also simulated at a temperature of 38ºC and compared with experimental measurements in the lab at the same temperature, as shown in Table 5-4. The agreement is satisfactory and within the range of available correlations for MMP.

Table 5-4: Comparison of multi-contact miscibility (MCM) pressure with experimental measurement at 38℃ using dead Bakken crude.

	Method of Characteristics	Method of Multiple-Mixing Cells	Experimental Measurement
MMP (psia)	1069.5	1175.5	1200

5.3. Rock-Fluid System

Relative permeability data were obtained from Kurtoglu's PhD thesis (2013) for a Middle Bakken core sample with absolute permeability of 0.015 md and porosity of 6.2%. Unsteady-state water-oil relative permeability experiment was performed by CoreLabs at 1600 psi of net confining stress and 70°F.

Three-phase relative permeability curves for a matrix system were generated using Brooks-Corey's equations, based on parameters given in Table 5-5 (Kurtoglu, 2013). Capillary pressure was neglected in the simulation due to lack of laboratory test data.

Figure 5-4 plots matrix relative permeability data in both water-oil and gas-oil systems.

Table 5-5: Parameters used to generate relative permeability curves for matrix system in CMG simulator by Brooks-Corey Equations (Kurtoglu, 2013).

Matrix System			
Water-Oil		Gas-Oil	
krw	0.024	krg	0.096
krow	0.103	krog	0.106
Swr	0.531	Slg	0.730
Sorw	0.211	Sgr	0
nw	1.5	ng	2
no	2.5	nog	2.5

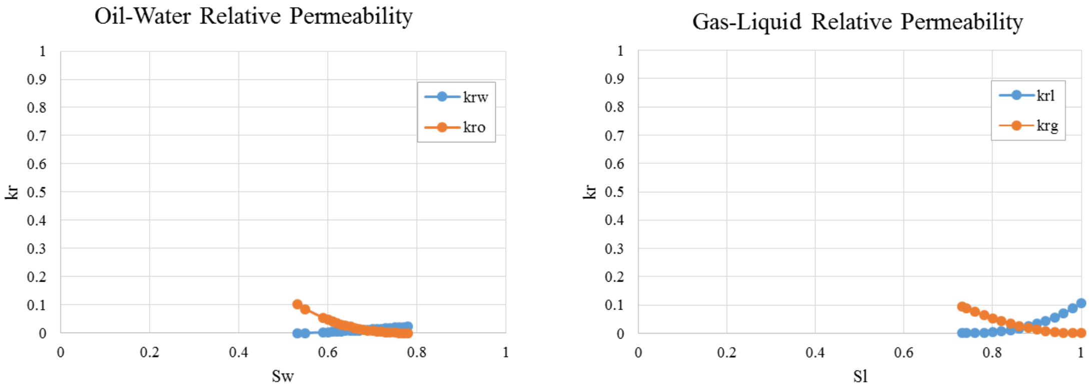

(a) (b)

Figure 5-4: Water-oil and gas-liquid relative permeability data for matrix system.

5.4. Molecular Diffusion

Gas or liquid, single-phase (*k*) binary molecular diffusion coefficient, D_{ij}, was modeled using the Sigmund (1976) correlation:

$$D_{ij} = \frac{\rho_k^0 D_{ij}^0}{\rho_k}(0.99589 + 0.096016\,\rho_{kr} - 0.22035\,\rho_{kr}^2 + 0.032874\,\rho_{kr}^3) \qquad (5\text{-}1)$$

where ρ_{kr} is the reduced mixture density for phase *k*, at the average mole fraction of component I defined by:

$$\rho_{kr} = \rho_k \left(\frac{\sum_{i=1}^{n_c} y_{ik} v_{ci}^{5/3}}{\sum_{i=1}^{n_c} y_{ik} v_{ci}^{2/3}} \right) \tag{5-2}$$

where y_{ik} is the molar fraction of component i in the mixture k, v_{ci} is the critical molar volume of component i, and $\rho_k^0 D_{ij}^0$ is the zero-pressure limit of the density-diffusivity product, given by the following expression of Chapman-Enskog dilute as theory:

$$\rho_k^0 D_{ij}^0 = \frac{0.0018583\, T^{1/2}}{\sigma_{ij}^2 \Omega_{ij} R} \left(\frac{1}{M_i} + \frac{1}{M_j} \right)^{1/2} \tag{5-3}$$

In the above equations, M is molecular weight, T is temperature, and R is the universal gas constant. The collision diameter σ_{ij} and the collision integral Ω_{ij} of the Lennard-Jones potential are related to component critical properties through the following equations:

$$\sigma_i = (2.3551 - 0.087\,\omega_i) \left(\frac{T_{ci}}{P_{ci}} \right)^{1/3} \tag{5-4}$$

$$\varepsilon_i = k_B (0.7915 + 0.1963\,\omega_i) T_{ci} \tag{5-5}$$

$$\sigma_{ij} = \frac{\sigma_i + \sigma_j}{2} \tag{5-6}$$

$$\varepsilon_{ij} = \sqrt{\varepsilon_i \varepsilon_j} \tag{5-7}$$

$$T_{ij}^* = \frac{k_B}{\varepsilon_{ij}} \tag{5-8}$$

$$\begin{aligned} \Omega_{ij} &= 1.06306 \left(T_{ij}^* \right)^{-0.15610} + 0.19300 \exp(-0.47635\, T_{ij}^*) \\ &+ 1.03587 \exp(-1.52996\, T_{ij}^*) + 1.76474 \exp(-3.89411\, T_{ij}^*) \end{aligned} \tag{5-9}$$

where k_B is the Boltzmann's constant, w_i is acentric factor, T_{ci} and P_{ci} are critical temperature and pressure of component i, respectively. T_{ij}^* is reduced temperature. The diffusion of component i in the mixture k is:

$$D_{ik} = \frac{1 - y_{ik}}{\sum_{j \neq 1} y_{ik} D_{ij}^{-1}} \tag{5-10}$$

Sigmund's correlation is the product of a study that included experimental work with binary systems in which the observed and compiled diffusion coefficients were fitted through a polynomial equation in reduced density. Density-diffusivity product is evaluated at a zero-pressure limit.

5.5. Discussion of History Matching Results

Figure 5-5 shows that the compositional simulation model has the tendency to match closely the overall oil production and recovery, but not the early recovery period where CO_2 diffusion is seen as a major recovery mechanism. It is also observed that the simulation model has a larger displacement efficiency, possibly due to the following simplified assumptions:

- Matrix heterogeneities were neglected in a single porosity-permeability model.
- In the simulation, a slimtube model was implemented to mimic linear flow commonly observed in coreflood experiments. The flow regime parallel to the core face was not captured. However, the presence of an "artificial" fracture inside the core matrix promotes flow in the direction perpendicular to core length.

Figure 5-6 shows that CO_2 injection re-pressurizes the core matrix, thereby re-establishing a drive mechanism dominant by advection. Both wells are controlled by constant bottom-hole pressure (BHP).

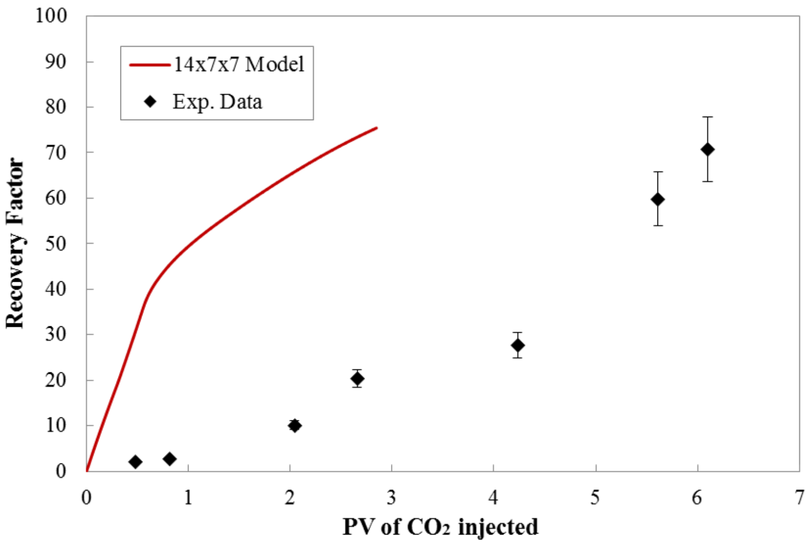

Figure 5-5: History-match of Bakken hydrocarbon recovery with CO_2 solvent, using a base model of 14 x 7 x 7.

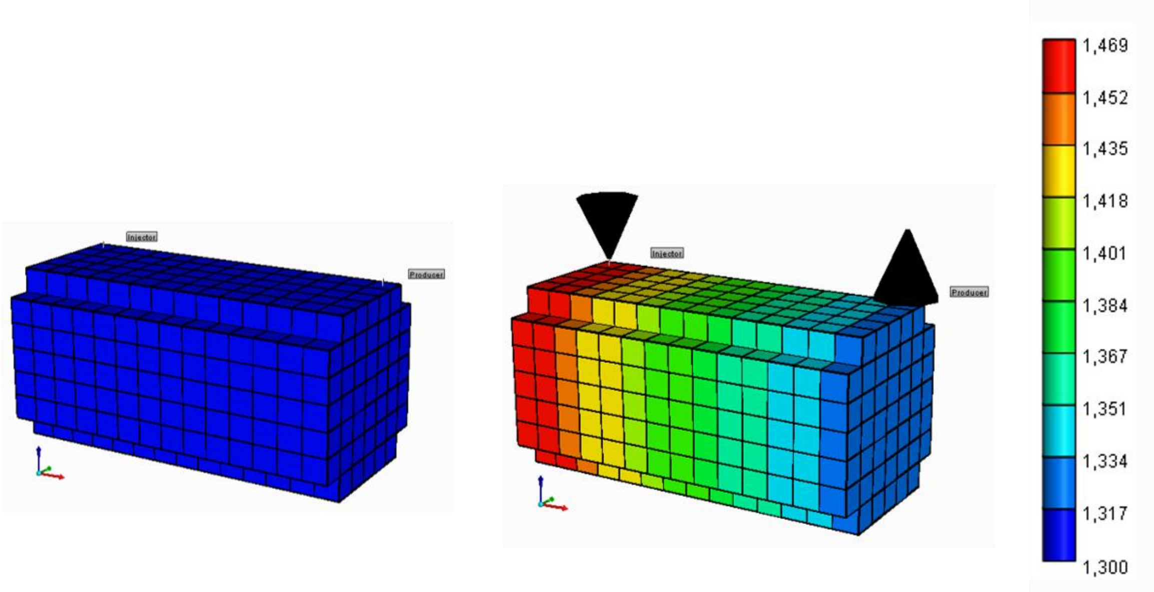

Figure 5-6: Pressure distribution from simulation of miscible CO_2 injection. Left: initial condition; Right: constant BHP well control.

Figure 5-7 and 5-8 present a temporal and spatial development of gas/oil saturation from the simulation model. Initial oil saturation is 1. Figure 5-9 shows evolution of global molar CO_2 fraction within the model as gas injection process progresses. The dead oil contains very little CO_2, therefore CO_2 fraction in the oil phase mainly comes from the injection gas stream. As more CO_2 dissolves in oil, the oil starts to swell which leads to reduction in viscosity, as shown in Figure 5-10. It is also observed that CO_2 permeates into the core matrix from the 1st layer where the injection well is completed. There is a zone of high CO_2 saturation that serves as a useful start to the diffusive process.

Light hydrocarbon components are preferentially extracted and produced whereas heavier components are left behind by the solvent + oil front. This is reflected through an increase in oil molar density, shown in Figure 5-11.

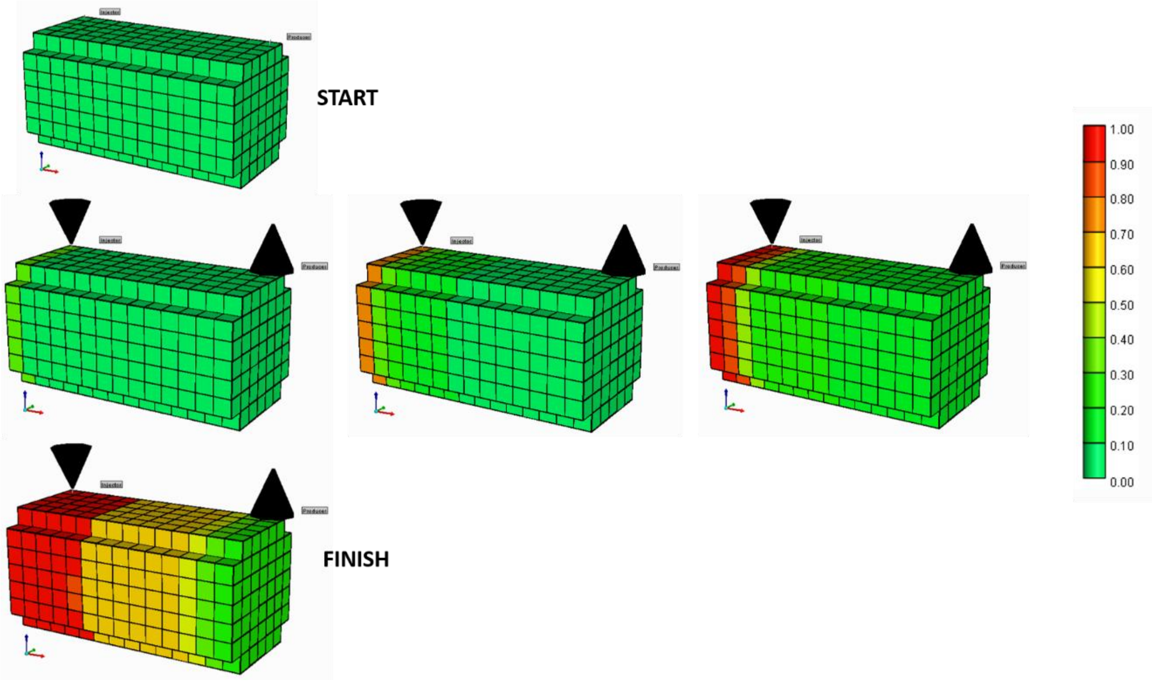

Figure 5-7: Gas saturation map from simulation of miscible CO_2 injection.

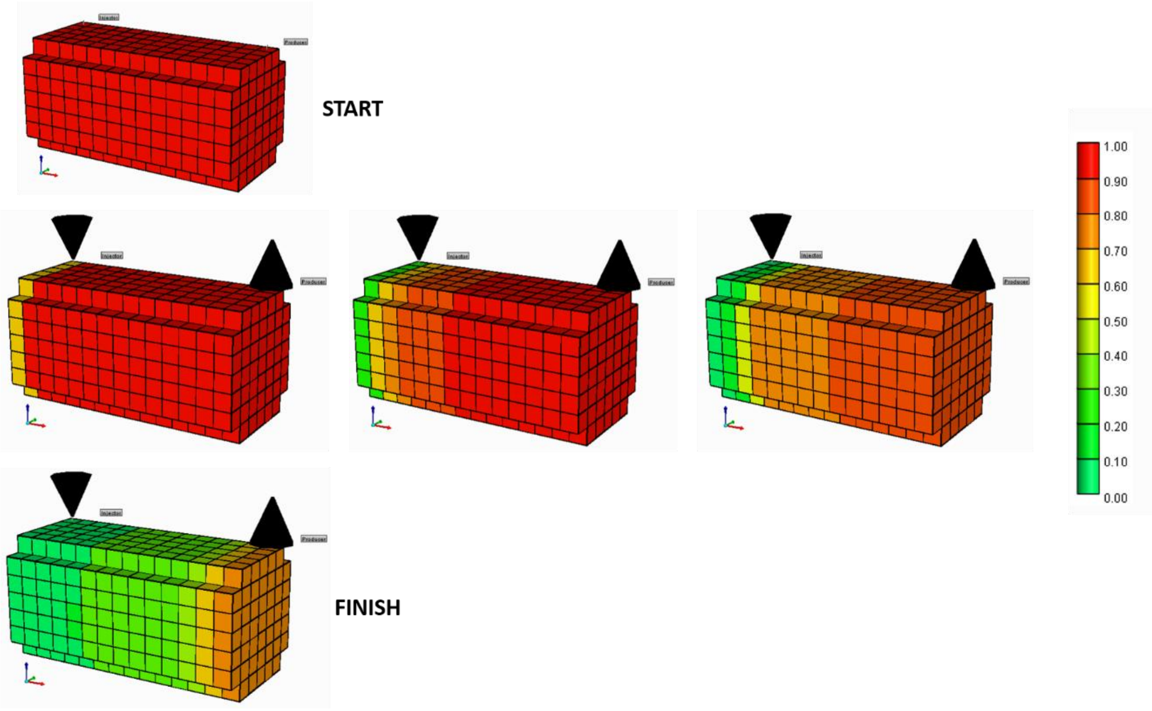

Figure 5-8: Oil saturation map from simulation of miscible CO_2 injection.

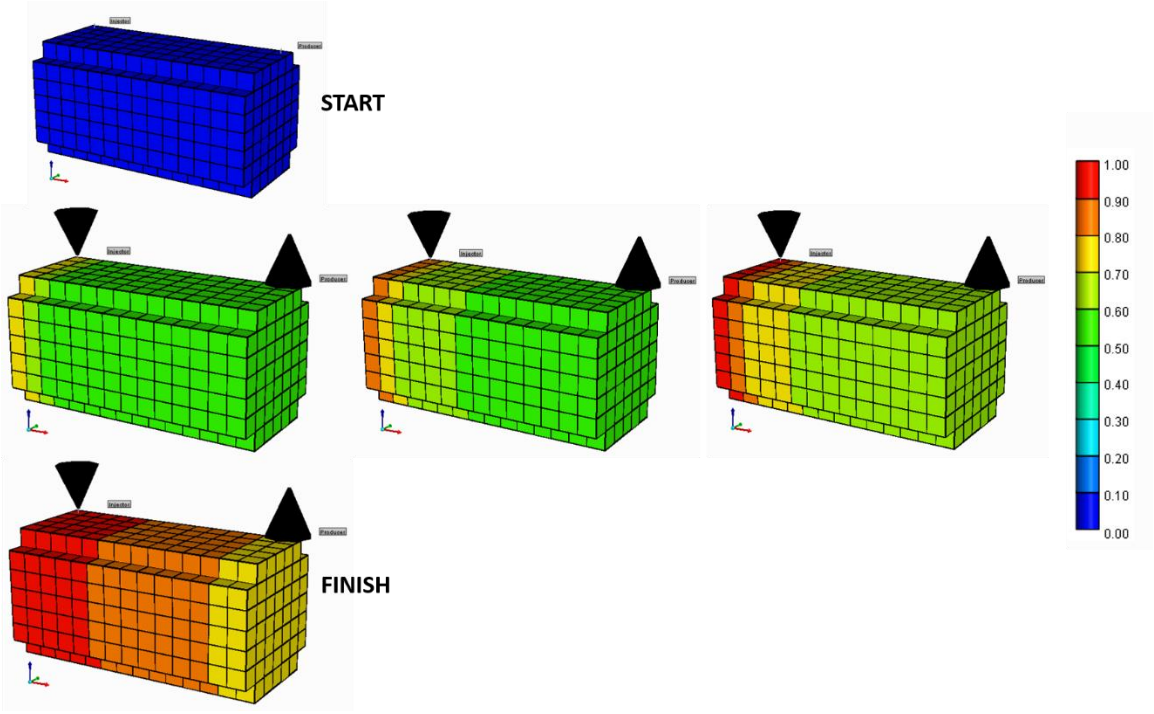

Figure 5-9: Global CO_2 molar fraction from simulation of miscible CO_2 injection.

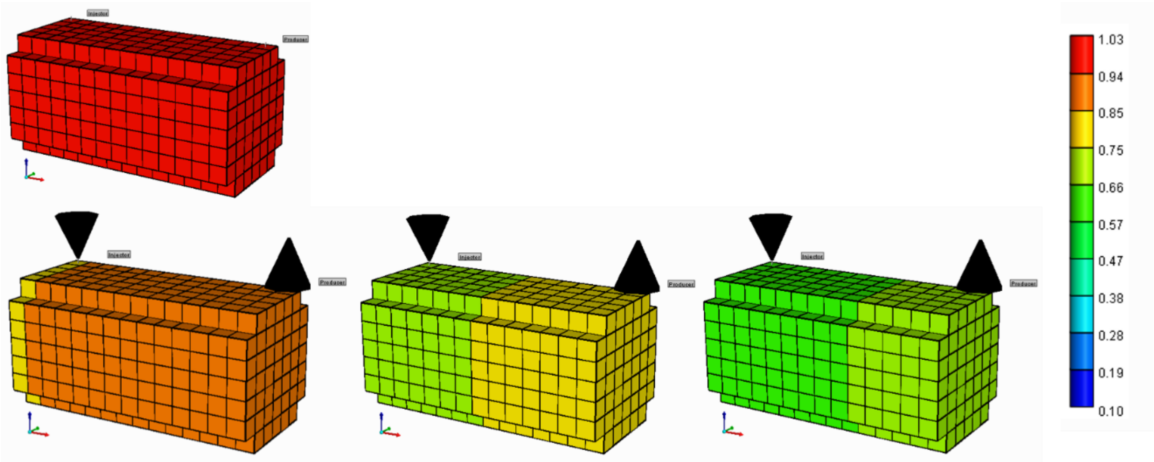

Figure 5-10: Oil viscosity from simulation of miscible CO_2 injection.

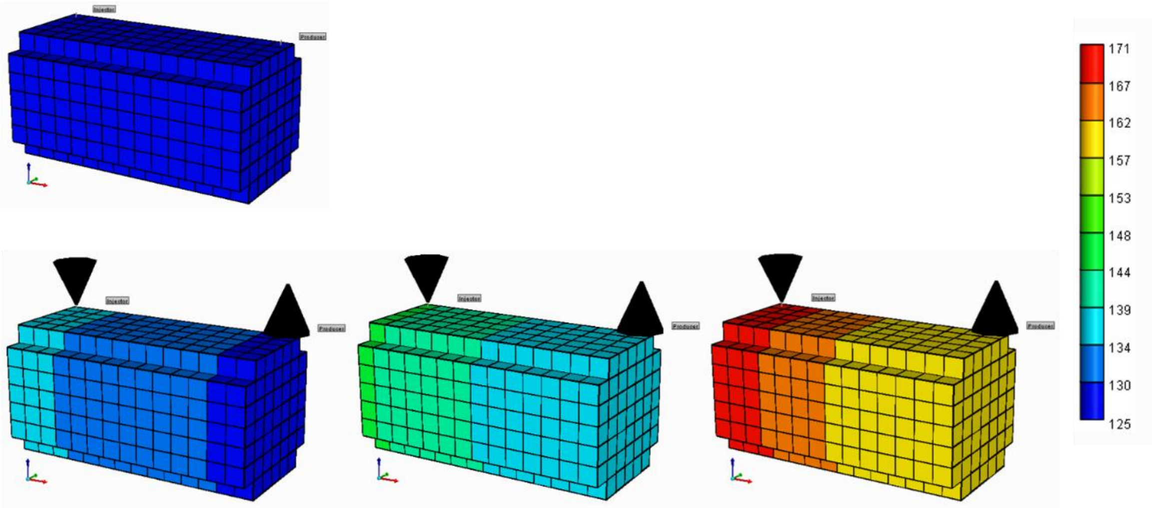

Figure 5-11: Oil molar density from simulation of miscible CO_2 injection.

Chapter 6

6. Conclusions and Future Work

Technical feasibility of enhanced oil recovery in a liquids-rich shale reservoir is evaluated on the laboratory scale and from a compositional flow simulation model. The following conclusions are made based on preliminary findings:

- Preferential extraction of light HC components into CO_2 appears to be the main mechanism for incremental oil production in a miscible CO_2 flood for tight-oil cores. Other controlling factors include re-pressurization, oil swelling, viscosity and interfacial tension reduction, as supported by both experimental observations and simulation efforts.

- The oil recovery potential of miscible CO_2 injection remains challenged by factors such as low permeability and rock heterogeneities; however, experimental results do indicate that miscible CO_2 injection is a technically feasible EOR method based upon encouraging increase in recovery and relatively rapid oil production obtained in the laboratory.

- The existence of fractures aids the transport process of CO_2. CO_2 penetrates from the fracture into the matrix through a diffusive mechanism and mix with oil to achieve miscibility.

- The impact of CO_2 penetration is more pronounced at a smaller energy of 80 keV due to contribution of photoelectric absorption to X-ray attenuation.

- During early recovery, we observe a decreasing trend of CT number with increasing volumes of CO_2 injected. However, the trend is reversed as CO_2 continues to invade the pore space. We have less changes in CT number towards greater recovery factors. One possible explanation is due to increased densities of the residual oil that has been left behind and mostly consist of heavier HC components. This speculation is also supported through simulation study on evolution of oil molar density with time.

- The history match achieved in the simulation study agrees closely with total oil production but the processes are not exactly matched. This is probably due to negligence of rock heterogeneities.

Looking forward, we plan to continue working on the following aspects:

- Conduct more coreflood experiments to obtain good volumetric data on oil recovery by CO_2 solvent.

- Simulate presence of a conductive hydraulic fracture using loosely-packed glass beads surrounding the core matrix. This experimental design is more representative of the field development strategy currently used in unconventional tight-oil reservoirs.

- We always have this challenge of not getting enough CT contrast due to low porosity of Bakken core sample. Therefore, it is suggested to try:

    1. A longer X-ray exposure time to get more signal from the fluid.

    2. Dope the oil phase to maximize photoelectric effect.

- Perform sensitivity analysis on the following input parameters:

    1. Oil phase compressibility

    2. Relative permeability

    3. Diffusion coefficients from other available correlations

    4. Number of pseudo-components in the fluid model

Nomenclature

1.1 Abbreviation

OOIP	Original oil in place
TOC	Total organic content
EOR	Enhanced oil recovery
MMP	Minimum miscibility pressure
MME	Minimum miscibility enrichment
CT	Computed tomography
BPR	Back pressure regulator
BHP	Bottom-hole pressure

1.2 Notation

μ	Linear attenuation coefficient
ρ	Density
Z	Effective atomic number
ϕ	Porosity
CT_{or}	CT number of oil-saturated rock
CT_{ar}	CT number of air-saturated rock
CT_{oil}	CT number of oil
CT_{air}	CT number of air
R_f	Recovery factor
N_x	Number of grid blocks in x direction
N_y	Number of grid blocks in y direction
N_z	Number of grid blocks in z direction
P_c	Critical pressure, atm
T_c	Critical temperature, K
MW	Molecular weight, g/mol

References

Akin, S. and Kovscek, A.R., 2003. “Computed Tomography in Petroleum Engineering Research”. Applications of X-ray Computed Tomography in the Geosciences, Geological Society, London, Special Publications, 215, 23-28.

Alharthy, N., et al., 2015. “Enhanced Oil Recovery in Liquid-Rich Shale Reservoirs: Laboratory to Field”. Paper SPE 175034 presented at the SPE Annual Technical Conference and Exhibition held in Houston, Texas, USA, September 28-30, 2015.

Anonymous, 2012. “Survey: Miscible CO2 now eclipses steam in US EOR production”. Oil & Gas Journal, 110, 56-57.

Beliveau, D.A., 1987. “Midale CO2 Flood Pilot”. Journal of Canadian Petroleum Technology, 26(6). Doi: 10.2118/87-06-05.

Gaswirth, S.B., Marra, K.R., Cook, T.A., Charpentier, R.R., Gautier, D.L., Higley, D.K., Klett, T.R., Lewan, M.D., Lillis, P.G., Schenk, C.J., Tennyson, M.E., and Whidden, K.J., 2013. “Assessment of Undiscovered Oil Resources in the Bakken and Three Forks Formations, Williston Basin Province, Montana, North Dakota, and South Dakota, 2013 U.S. Geological Survey Fact Sheet 2013-3013”. U.S. Geological Survey: Denver, CO.

Harju, J., 2012. “Bakken and CO2”. Presentation at North Dakota Petroleum Council Annual Meeting held in Medora, North Dakota, USA, September.

Hoffman, B. Todd, 2012. “Comparison of Various Gases for Enhanced Recovery from Shale Oil Reservoirs”. Paper SPE 154329 presented at the SPE Improved Oil Recovery Symposium, Tulsa, OK.

Kurtoglu, B., Sorensen, J.A., Braunberger, J., Smith, S., Kazemi, H., 2013. “Geological Characterization of a Bakken Reservoir for Potential CO2 EOR”, paper SPE 168915 presented at the Unconventional Resources Technology Conference held in Denver, Colorado, USA, August 12-14.

Kurtoglu, B., 2013. “Integrated Reservoir Characterization and Modeling in Support of Enhanced Oil Recovery for Bakken”, Ph.D. Dissertation, Colorado School of Mines.

Liu, G., Sorensen, J.A., Braunberger, J.R., Klenner, R., Ge, J., Gorecki, C.D., Steadman, E.N., Harju, J.A., 2014. “CO2-Base Enhanced Oil Recovery from Unconventional Reservoirs: A Case Study of the Bakken Formation”. Paper SPE 168979 presented at the SPE Unconventional Resources Conference – USA held in the Woodlands, Texas, USA, April 1-3.

Mohanty, K., Chen, C., Balhoff, M., 2013. “Effect of Reservoir Heterogeneity on Improved Shale Oil Recovery by CO2 Huff-n-Puff”. Paper SPE 164553 presented at the SPE Unconventional Resources Conference held in the Woodlands, TX.

MHRA Evaluation Report, 2003. “GE Lightspeed Ultra Advantage: CT Scanner Technical Evaluation”. MHRA 03066.

Nordeng, S.H. et al., 2008. “State of North Dakota - Bakken Formation Resource Study Project”. North Dakota Department of Mineral Resources, April 2008.

Pedersen, K.S., A.L. Blilie, and K.K. Meisingset, 1992. “PVT Calculations on Petroleum Reservoir Fluids Using Measured and Estimated Compositional Data for the Plus Fraction”. Ind. Eng. Chem. Research, 31(5), 1378-1384.

Poellitzer, S., Florian, T., & Clemens, T., 2009. “Revitalising a Medium Viscous Oil Field by Polymer Injection, Pirawarth Field, Austria”. Paper SPE 120991 presented at EUROPEC/EAGE Conference and Exhibition, 8-11 June, Amsterdam, The Netherlands. doi: 10.2118/120991-MS.

Rao, D., 2001. “Gas Injection EOR- A New Meaning in the New Millennium. Petroleum Society of Canada”. doi: 10.2118/01-02-DAS.

Sahin, Secaeddin, Kalfa, Ulker, and Celebioglu, Demet, 2008. “Bati Rman Field Immiscible CO2 Application – Status Quo and Future Plans”. SPE Reservoir Evaluation & Engineering, 11(4), pp. 778-791. Doi: 10.2118/106575-pa.

Shoaib, S., Hoffman, B. Todd, 2009. “CO2 Flooding the Elm Coulee Field”. Paper SPE 123176 presented at the SPE Rocky Mountain Petroleum Technology Conference held in Denver, CO, April 14-16.

Sorensen, J.A., Schmidt, D., Smith, S.A., Bailey, T.P., Mibeck, B.A.A., Harju, J.A. 2010. “Energy and Environmental Research Center Subtask 1.2-Evaluation of Key Factors Affecting Successful Oil Production in the Bakken Formation, North Dakota”. DOE Award No: DE-FC26-08NT43291, May 2010.

Taber, J. J., Martin, F. D., & Seright, R. S., 1997. “EOR Screening Criteria Revisited - Part 1: Introduction to Screening Criteria and Enhanced Recovery Field Projects”. Society of Petroleum Engineers. doi: 10.2118/35385-PA.

Theloy, C., 2014. “Integration of Geological and Technological Factors Influencing Production in the Bakken Play”. Ph.D. Dissertation, Colorado School of Mines.

Tovar, F.D. et al., 2014. “Experimental Investigation of Enhanced Recovery in Unconventional Liquid Reservoir using CO2: A Look Ahead to the Future of Unconventional EOR”. Paper 169022 presented at the SPE Unconventional Resources Conference held in the Woodlands, Texas, April 1-3.

Tran, T., Sinurat, P., and Wattenbarger, R.A., 2011. “Production Characteristics of the Bakken Shale Oil”. Paper SPE 145684 presented at the SPE Annual Technical Conference and Exhibition, Denver, CO, USA, 30 October-2 November.

Vega, B., O’Brien, W.J., Kovscek, A.R., 2010. “Experimental Investigation of Oil Recovery from Siliceous Shale by Miscible CO2 Injection”. Paper SPE 135627 presented at the SPE Annual Technical Conference and Exhibition, Florence, Italy.

Vinegar, H.J., Wellington, S.L., 1987. “Tomographic Imaging of Three-Phase Flow Experiments”, Review of Scientific Instruments, 58(1), 96.

U.S. Energy Information Administration, 2013. “Annual Energy Outlook 2013”, Washington, DC.

Appendix A

A. Pure Fluid CT Number

Because liquid is incompressible, changes in CT number of liquid such as oil are almost negligible at different pressures. For convenience, CT number of dead oil was obtained at ambient pressure and 38°C. It is averaged as -177.4. Unlike oil, the CT number of CO_2 changes dramatically with pressure, especially at its supercritical state. Therefore, a range of pressures from 900 psi to 1600 psi was tested with temperature fixed at 38°C.

As shown in Figure A-1, a jump in average CT number is observed when pressure transitions from 1100 psi to 1200 psi. This corresponds to the fact that the critical pressure of CO_2 is slightly above 1000 psi. Therefore, when CO_2 becomes supercritical, its CT number increases.

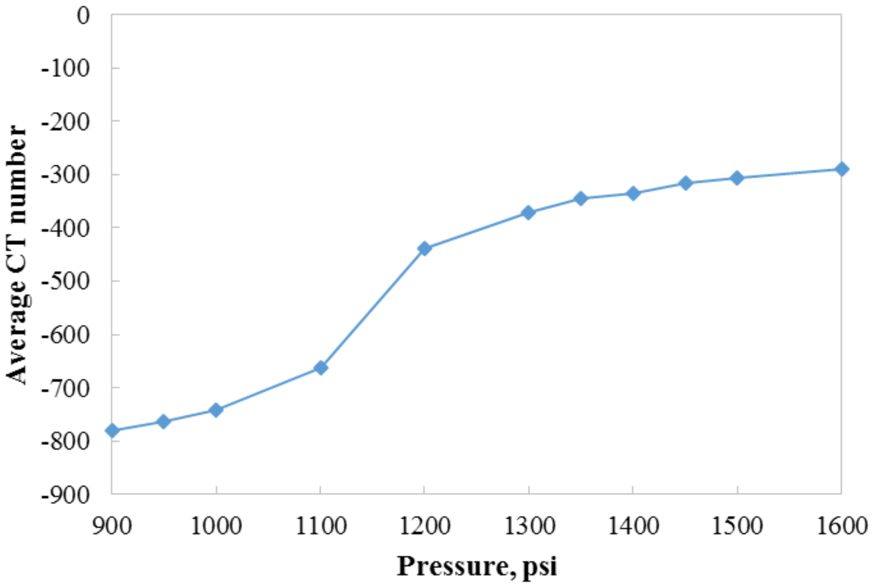

Figure A-1: Pure fluid CT number of CO_2 at varying pressures and fixed temperature at 38°C.

Appendix B

B. CT Image Analysis

Figure B-1 plots the average CT number as a function of pore volume of CO_2 injected at an energy level of 140keV and 80keV. Note that the CT number shown in Figure B-1 is averaged from a total of 45 images at each time, and a PVI of zero is equivalent to oil-saturated core before any penetration of CO_2. Initially, at both energy levels, the CT number decreases with increasing volume of CO_2 but this decreasing trend is somehow reversed as more CO_2 continues to invade the pore space. The last data point corresponding to a recovery factor of 71% actually has a greater CT number, in comparison to the oil-saturated image. It is reasonable to speculate that at a larger recovery factor, most of the light components in the oil mixture have been preferentially produced which leaves behind the heavier components. This may result in an increase of density from residual oil when compared with original oil that has both light and heavy components.

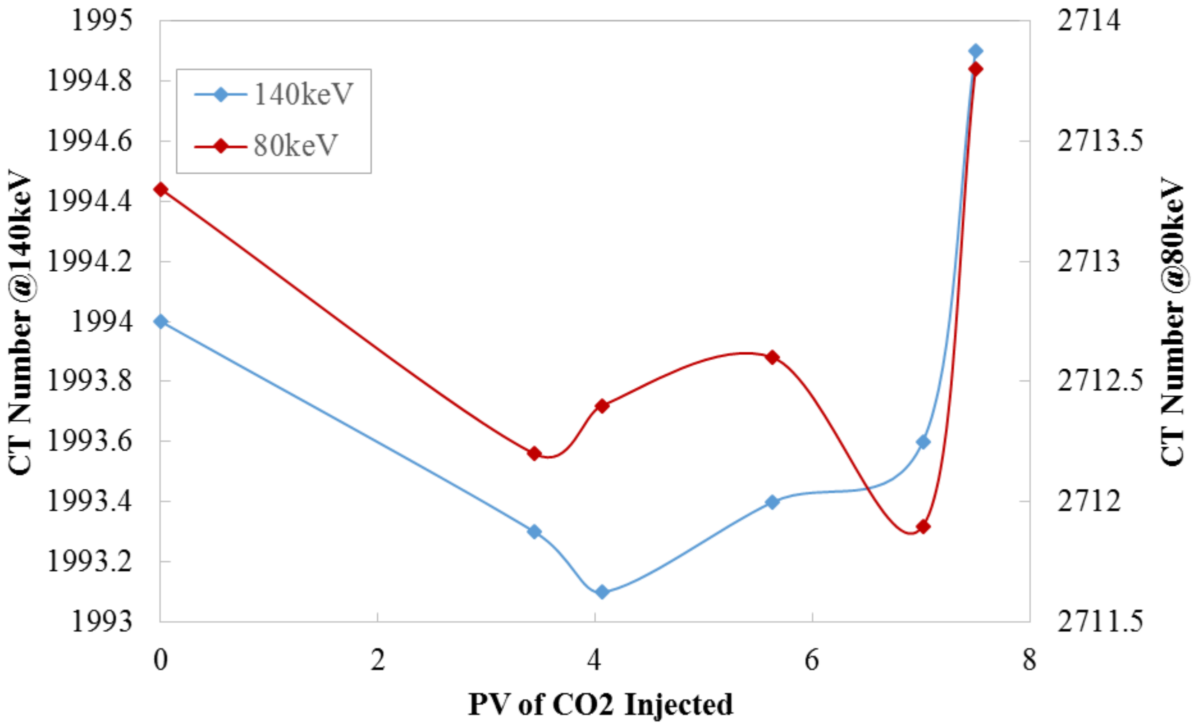

Figure B-1: Average CT number as a function of pore volume of CO_2 injected. The y-axis on the left represents CT number at 140 keV; the y-axis on the right represents CT number at 80 keV.

In Figure B-2, we specifically focus on comparisons between recovery factors at two ends of the spectrum: R_f =20% and R_f=71%. The x-axis is translated into relative distance to injection face using a number of slices and 1mm thickness per slice. Small changes of CT number are apparent around the fracture region, but not so much elsewhere. This is probably because the core has such a low porosity that not enough signal is captured from the fluid and any small differences are most likely to be buried in by averaging throughout the whole slice.

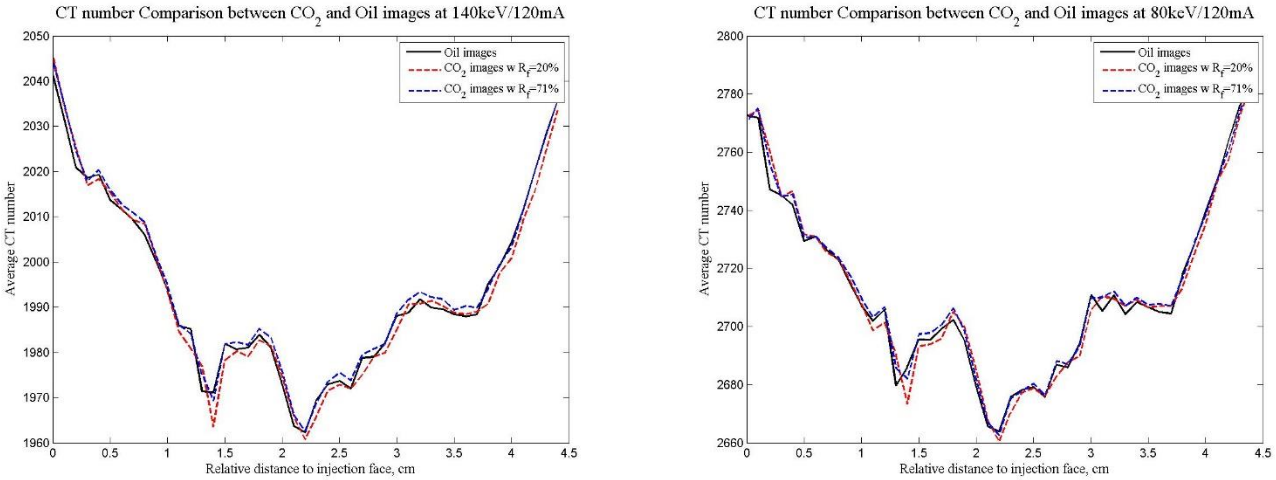

(a) (b)

Figure B-2: CT number comparison between oil and CO_2 images as a function of relative distance to injection core face. (a) 140 keV/120 mA, (b) 80 keV/120 mA.

A theoretical CT number difference is calculated with given information in porosity distribution, pure fluid CT numbers and mass fraction of each component occupying the pore space in the context of miscibility. Mass fractions are found through recovery factor and fluid densities evaluated at the same T and P. The expressions are shown below:

$$CT = (1-\phi)\cdot CT_{rock} + \phi \cdot CT_{fluid} \tag{B-1}$$

$$\Delta CT = \phi \cdot (CT_{fluid}(t) - CT_{fluid}(t=0)) \tag{B-2}$$

$$CT_{fluid}(t) = x_{CO2} CT_{CO2} + (1-x_{CO2}) CT_{oil} \tag{B-3}$$

$$CT_{fluid}(t=0) = CT_{oil} \tag{B-4}$$

$$x_{CO2} = \frac{R_f \rho_{CO2}}{(1-R_f)\rho_{oil} + R_f \rho_{CO2}} \tag{B-5}$$

The purpose of this exercise is to check the quality of data obtained from coreflood experiments and CT imaging by comparing with a synthetic reconstruction based on theoretical understandings and simplified physics. In Figure B-3 (b), a 3-D porosity profile is used to compute a series of ΔCT at R_f= 20% and 71% based on Eq. (B-1) to (B-5) and fluid properties from Table B-1. As shown, in the theoretical calculation, the distribution of CT number differences shifts towards the more negative end at a larger recovery factor and the spread of the data set is wider in comparison to a smaller recovery factor. This suggests that as more oil is displaced out of the matrix, the empty pore space is occupied by CO_2 instead that results in a decrease of CT number for the core sample. Also, the change of CT number is up to -5 for R_f = 20% and -20 for R_f = 71%. In contrast, a different pattern is observed in Figure B-3 (a) from the experimental side:

- There is no apparent shift in CT number differences from R_f = 20% to 71%.

- The magnitude of changes in CT number are a lot larger than what is expected from theoretical calculations.

- There is an abundant presence of positive differences that may be a result of machine random error or increased density of residual oil that consists of heavier components.

Table B-1: Fluid properties for CO_2 and Bakken crude oil.

	Density g/mL	**Pure Fluid CT Number @140keV**
CO_2	0.616	-335.1
Oil	0.785	-177.4

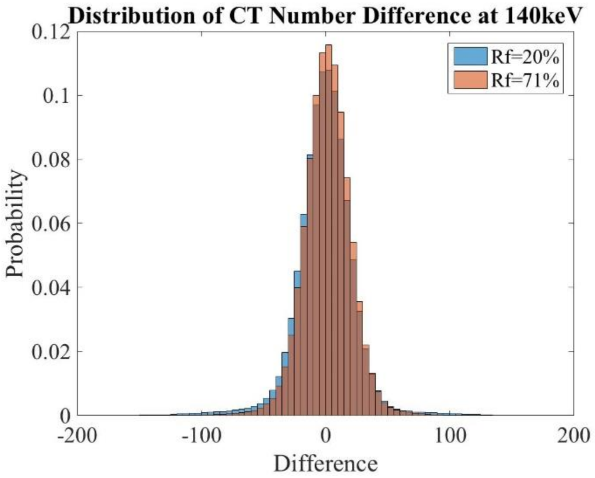

(a)

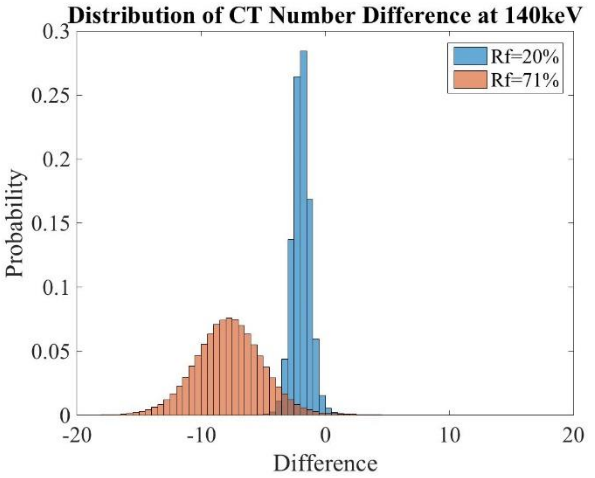

(b)

Figure B-3: Histogram on distribution of CT number differences with different recovery factors at 140 keV/120 mA. (a) Experimental measurement, (b) Theoretical calculation based on 3-D porosity profile of the core sample.

Figure B-4 provides a different perspective from Figure B-3. In particular, Figure B-4 reconstructs ΔCT at 140keV for a series of recovery factors from 10% to 71% using a constant average porosity value of 7.5%. The predicted ΔCTs are then compared with the averaged experimental results. In the process of analyzing experimental data, we only focus on negative CT differences and choose to eliminate 10% of data from the far negative side of the distribution before taking the average. As expected, theoretical prediction shows a linear increasing trend of CT number differences with respect to greater recovery factors. Experimental results, however, present a completely opposite pattern. We argue that one possible explanation is due to preferential extraction of lighter oil components into the CO_2 phase. If such is the case, then the underlying assumptions of constant oil and CO_2 densities may not be reflective of what is really happening at core level.

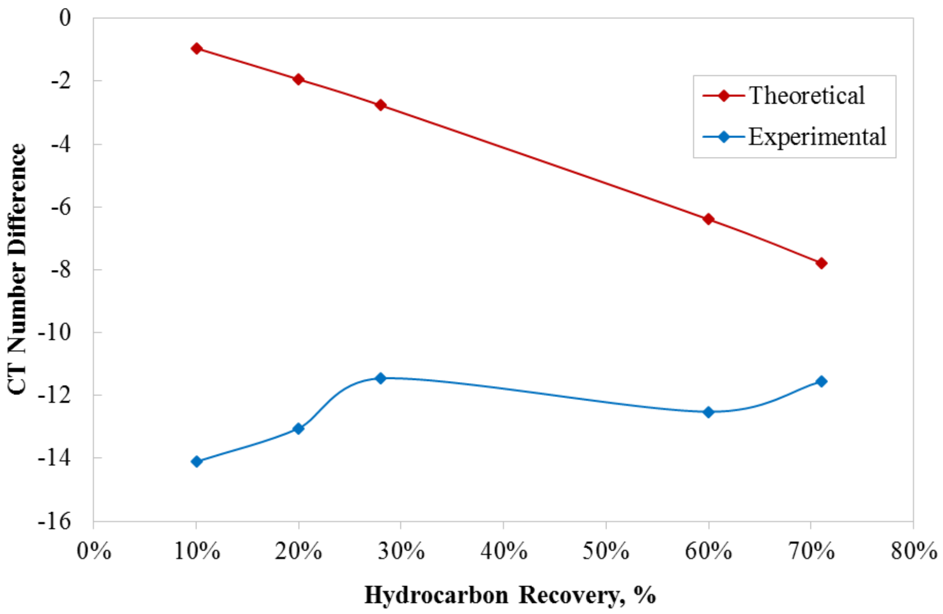

Figure B-4: Theoretical reconstruction of CT number differences at 140 keV/120 mA as a function of percentage of hydrocarbon recovery.

Appendix C

C. Sensitivity Analysis on Grid Refinement

This chapter presents sensitivity analysis on grid refinement using a simplified 1-D model with length and cross-sectional area identical to experimental values. The number of grid blocks in the flow direction is varied from 50 to 200 to study the effect of increasing number of grid cells on convergence and simulation run time.

Figure C-1 plots oil recovery as a function of pore volume of CO_2 injected for different numbers of grid blocks in the flow direction. The recovery curves look almost identical in spite of differences in size of the simulation model. 95% of the original oil is produced when more than 10 pore volumes of CO_2 have been injected. Majority of the efforts (6 pore volumes) are directed to recover the last 10% oil composed of heavier hydrocarbons.

Figure C-2 shows CPU time consumption and the total number of timesteps as a function of model size on a log-log plot. A linear interpolation of both parameters are made to estimate computation expenses of bigger models.

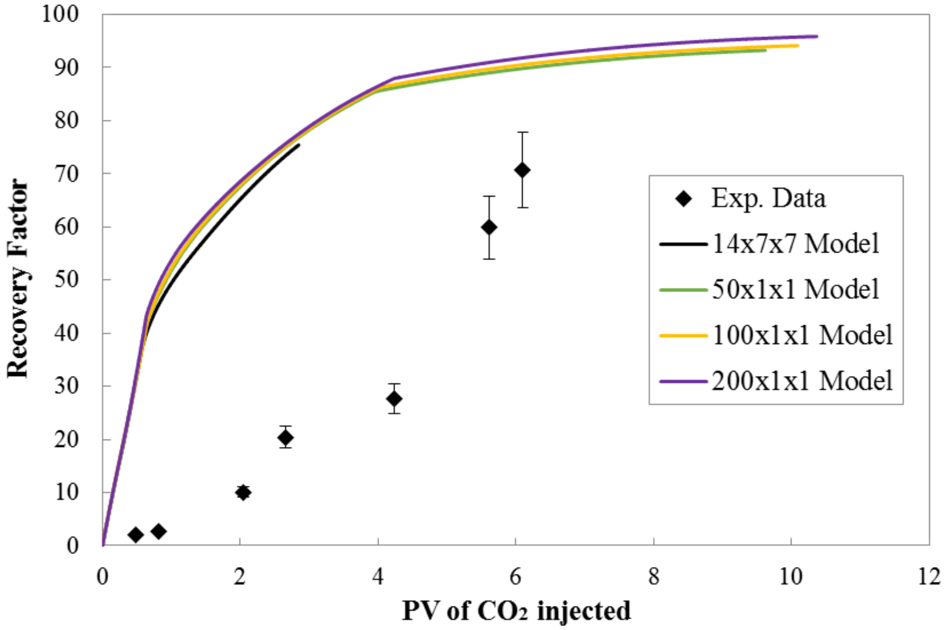

Figure C-1: Effect of grid refinement on convergence for a simulation time of 10 days (4 processors).

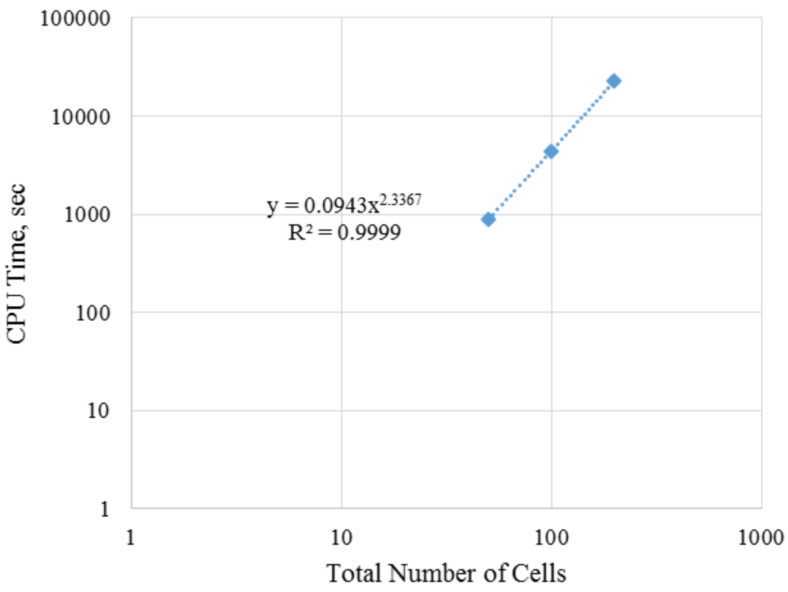

(a)

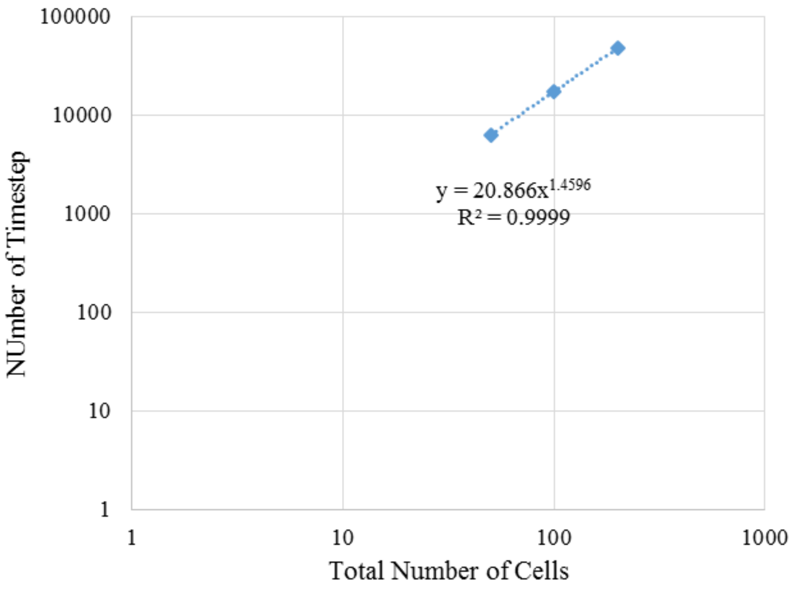

(b)

Figure C-2: Effect of grid refinement on numerical controls for a simulation time of 10 days (4 processors), (a) CPU time used, (b) Number of timesteps.

Appendix D

D. Miscible CO_2 Coreflood Experiment CMG GEM Input

Because this is a lab-scale problem, simulation has to be run at a tighter tolerance and also on fully-implicit formulation to avoid convergence issues, as shown in Table C-1.

Table D-1: Specifications of timestep control for a laboratory model.

Minimum time step size	1E-8 day
Maximum time step size	0.01 day
Maximum number of iterations per time step	200

Keyword *SLIMTUBE is used in the data input file to represent injection of CO_2 at one end and production of hydrocarbons from the other. A special well index calculation is performed in place of Peaceman's equation, as it is only valid for radial flow. Well index is given as:

$$wi^{'} = wi \cdot geofac \cdot wfrac \cdot k \cdot area \tag{C-1}$$

where *geofac* and *wfrac* are well geometric parameter and angular completion fraction as defined in keyword *GEOMETR, *wi* is dimensionless partial perforation factor usually set to 1, *k* is the perforated grid block permeability in the direction of slimtube flow and *area* is the grid block area perpendicular to the flow. The *SLIMTUBE option avoids some difficulties which arise in well index calculations due to small grid block size in slimtubes relative to usual well dimensions.

```
** 2016-05-19, 12:24:23 PM, kez
** 2016-05-19, 1:40:34 PM, kez
** 2016-05-19, 4:18:37 PM, kez
** 2016-05-19, 4:46:12 PM, kez
** 2016-05-31, 5:18:00 PM, kez
RESULTS SIMULATOR GEM 201210
*INUNIT  *FIELD
WSRF WELL 1
WSRF GRID TIME
OUTSRF GRID PRES RHOG RHOO SG SO SW VISG VISO XALL YALL ZALL
OUTSRF RES ALL
```

```
OUTSRF WELL LAYER ALL DOWNHOLE
WPRN GRID 0
OUTPRN GRID NONE
OUTPRN RES NONE

DIARY2 WELL-INFO

**$  Distance units: ft
RESULTS XOFFSET          0.0000
RESULTS YOFFSET          0.0000
RESULTS ROTATION          0.0000  **$  (DEGREES)
RESULTS AXES-DIRECTIONS 1.0 -1.0 1.0
**$
**************************************************************************
***
**$ Definition of fundamental cartesian grid
**$
**************************************************************************
***
GRID CART 14 7 7
KDIR DOWN
DI IVAR
 14*0.0119
DJ JVAR
 7*0.0119
DK KVAR
 7*0.0119
**$  0 = null block, 1 = active block
NULL CON            1

*POR  *ALL
*INCLUDE 'poro_I14.txt'

*PERMI  *ALL
*INCLUDE 'perm_I14.txt'** This include file must exist in the directory with the .dat file
otherwise the path must be included in the name
PERMJ EQUALSI
PERMK EQUALSI

**$  0 = pinched block, 1 = active block
PINCHOUTARRAY CON            1
PRPOR 1300
CPOR 5.54e-6
**The following is the fluid component
**property data in GEM format.
**The unit system and fluid compositions should
```

```
**be specified in the I/O control section.
**The units and compositions specified in WinProp
**are included here as comments for informational purposes.
** PVT UNITS CONSISTENT WITH *INUNIT *FIELD
**COMPOSITION *PRIMARY
**        6.7100000E-05  1.9613000E-03  8.4563000E-03  2.4611800E-02
**        4.3140100E-02  5.2754300E-02  5.9223600E-02  3.7768640E-01
**        1.6269780E-01  1.2592250E-01  6.7064500E-02  7.6414300E-02
**COMPOSITION *SECOND
**        0.0000000E+00  0.0000000E+00  0.0000000E+00  0.0000000E+00
**        0.0000000E+00  0.0000000E+00  0.0000000E+00  0.0000000E+00
**        0.0000000E+00  0.0000000E+00  0.0000000E+00  0.0000000E+00
**$ Model and number of components
MODEL PR
NC 12 12
COMPNAME 'CO2' 'N2 toCH4' 'C2H6' 'C3H8' 'IC4toNC4' 'IC5toNC5' 'FC6' 'C07-C10'
'C11-C13' 'C14-C17' 'C18-C21' 'C22+'
HCFLAG
0 0 0 0 0 0 0 0 0 0 0 0
VISCOR MODPEDERSEN
VISCOEFF    1.3040000E-04    2.0087946E+00    7.3780000E-03    1.7367009E+00
4.1384000E-01
MW
4.4010000E+01   1.6577972E+01   3.0070000E+01   4.4097000E+01   5.8124000E+01
7.2151000E+01   8.6000000E+01   1.3776000E+02   1.9820000E+02   2.5558000E+02
3.2290000E+02 3.4496625E+02
AC
0.225 0.00943017 0.098 0.152 0.189388 0.242127 0.27504 0.320515 0.459503 0.575118
0.701335 1.1184
PCRIT
7.2800000E+01   4.4893084E+01   4.8200000E+01   4.1900000E+01   3.7174961E+01
3.3339152E+01   3.2460000E+01   2.5149000E+01   2.0219000E+01   1.7146000E+01
1.5741706E+01 1.0573877E+01
VCRIT
9.4000000E-02    9.8568601E-02    1.4800000E-01    2.0300000E-01    2.5669311E-01
3.0473894E-01    3.4400000E-01    4.4546605E-01    6.2462892E-01    7.7817561E-01
9.4355957E-01 1.2372095E+00
TCRIT
3.0420000E+02   1.8758650E+02   3.0540000E+02   3.6980000E+02   4.2149216E+02
4.6618086E+02   5.0750000E+02   6.2721000E+02   6.8413806E+02   7.3342365E+02
7.9136392E+02 1.0669100E+03
PCHOR
78 75.3911 108 150.3 188.115 229.097 250.109 330.422 462.083 576.747 698.46 912.346
SG
0.818  0.314966  0.356  0.507  0.579407  0.628768  0.69  0.762497  0.811004  0.844424
0.874908 0.926648
```

```
TB
-109.21 -247.33 -127.57 -43.69 26.6524 91.369 146.93 262.185 408.898 520.761 630.824
835.956
OMEGA
0.457236 0.457236 0.457236 0.457236 0.457236 0.457236 0.457236 0.457236 0.457236
0.457236 0.457236 0.457236
OMEGB
0.0777961 0.0777961 0.0777961 0.0777961 0.0777961 0.0777961 0.0777961 0.0777961
0.0777961 0.0777961 0.0777961 0.0777961
VSHIFT
-0.0817  -0.160855  -0.1134  -0.0863  -0.071091  -0.0469502  -0.0591679  0.00368951
0.052204 0.075208 0.099845 0.0868319
HEATING_VALUES
0 806.556 1478.46 2105.16 2711.54 3353.66 3975.91 0 0 0 0 0
BIN
0.0000000E+00
0.0000000E+00 4.1185735E-03
0.0000000E+00 1.2932702E-02 0.0000000E+00
0.0000000E+00 2.2547806E-02 0.0000000E+00 0.0000000E+00
0.0000000E+00 3.1167124E-02 0.0000000E+00 0.0000000E+00 0.0000000E+00
0.0000000E+00    3.8034135E-02    0.0000000E+00    0.0000000E+00    0.0000000E+00
0.0000000E+00
1.5000000E-01    5.4735178E-02    0.0000000E+00    0.0000000E+00    0.0000000E+00
0.0000000E+00 0.0000000E+00
1.5000000E-01    8.0493426E-02    0.0000000E+00    0.0000000E+00    0.0000000E+00
0.0000000E+00 0.0000000E+00 0.0000000E+00
1.5000000E-01    9.9391310E-02    0.0000000E+00    0.0000000E+00    0.0000000E+00
0.0000000E+00 0.0000000E+00 0.0000000E+00 0.0000000E+00
1.5000000E-01    1.1720490E-01    0.0000000E+00    0.0000000E+00    0.0000000E+00
0.0000000E+00 0.0000000E+00 0.0000000E+00 0.0000000E+00 0.0000000E+00
1.5000000E-01    1.4399339E-01    0.0000000E+00    0.0000000E+00    0.0000000E+00
0.0000000E+00    0.0000000E+00    0.0000000E+00    0.0000000E+00    0.0000000E+00
0.0000000E+00

TRES 100
PHASEID TCMIX
DIFCOR-OIL SIGMUND
DIFCOR-GAS SIGMUND

ROCKFLUID
RPT 1
**$       Sw          krw         krow      Pcow
SWT
       0.531           0        0.103         0
        0.55  0.000479636   0.08507123         0
        0.59  0.002624579  0.053817145         0
```

```
       0.6  0.003319367  0.047308859         0
      0.61  0.004066514  0.041297193         0
      0.62  0.004862579  0.035768829         0
      0.63  0.005704722  0.030710067         0
      0.64  0.006590547  0.026106799         0
      0.65  0.007517997  0.021944463         0
      0.66  0.008485281     0.018208         0
      0.67  0.009490823  0.014881797         0
      0.68  0.010533218  0.011949623         0
      0.69  0.011611207  0.009394549         0
       0.7  0.012723651  0.007198848         0
      0.71  0.013869514  0.005343868         0
      0.72  0.015047848  0.003809875         0
      0.73  0.016257782  0.002575835         0
      0.74  0.017498512  0.001619117         0
      0.75   0.01876929   0.00091506         0
      0.76  0.020069424  0.000436298         0
      0.77  0.021398264   0.00015159         0
      0.78  0.022755202  2.34096E-05         0
     0.789        0.024            0         0
**$        Sl          krg        krog      Pcog
SLT
      0.73        0.096            0         0
      0.74  0.089020576  2.79831E-05         0
      0.76  0.075851852  0.000436214         0
      0.78  0.063736626  0.001564305         0
       0.8  0.052674897  0.003627785         0
      0.82  0.042666667  0.006799903         0
      0.84  0.033711934  0.011229959         0
      0.86    0.0258107  0.017051196         0
      0.88  0.018962963  0.024385103         0
       0.9  0.013168724  0.033344081         0
      0.92  0.008427984  0.044033221         0
      0.94  0.004740741  0.056551573         0
      0.96  0.002106996  0.070993084         0
      0.98  0.000526749  0.087447314         0
         1            0        0.103         0
KROIL STONE2 SO
INITIAL

USER_INPUT
PRES CON         1300
SW CON           0
ZGLOBALC 'N2 toCH4' CON     0.001961
ZGLOBALC 'IC5toNC5' CON      0.05275
ZGLOBALC 'IC4toNC4' CON      0.04314
```

```
ZGLOBALC 'FC6' CON     0.059224
ZGLOBALC 'CO2' CON    6.71E-005
ZGLOBALC 'C3H8' CON     0.024612
ZGLOBALC 'C2H6' CON     0.008456
ZGLOBALC 'C22+' CON     0.076414
ZGLOBALC 'C18-C21' CON     0.067065
ZGLOBALC 'C14-C17' CON     0.125923
ZGLOBALC 'C11-C13' CON     0.162698
ZGLOBALC 'C07-C10' CON     0.377686
TEMPER CON          100

NUMERICAL
DTMIN 1e-8
DTMAX 0.01
ITERMAX 200
NORTH 80
NORM PRESS 1000
NORM SATUR 0.05
NORM GMOLAR 0.005

RUN
DATE 2016 1 1
DTWELL 1e-7
AIMSET CON 3
**$
WELL  'Injector'
INJECTOR 'Injector'
INCOMP  SOLVENT  1.0  0.0  0.0  0.0  0.0  0.0  0.0  0.0  0.0  0.0  0.0  0.0
OPERATE  MAX  BHP  1500.0  CONT
**$          rad  geofac  wfrac  skin
GEOMETRY  K  0.003  0.37  1.0  0.0
PERF  *SLIMTUBE   'Injector'
**$ UBA      wi   Status  Connection
*include 'inlet_I14.txt'


WELL  'Producer'
PRODUCER 'Producer'
OPERATE  MIN  BHP  1300.0  CONT
**$          rad  geofac  wfrac  skin
GEOMETRY  K  0.003  0.37  1.0  0.0
PERF  *SLIMTUBE   'Producer'
**$ UBA      wi   Status  Connection
*include 'outlet_I14.txt'

DATE 2016 1 1.2
```

```
DATE 2016 1 1.4
DATE 2016 1 1.6
DATE 2016 1 1.8
DATE 2016 1 2
DATE 2016 1 2.2
DATE 2016 1 2.4
DATE 2016 1 2.6
DATE 2016 1 2.8
DATE 2016 1 3
DATE 2016 1 3.2
DATE 2016 1 3.4
DATE 2016 1 3.6
DATE 2016 1 3.8
DATE 2016 1 4
DATE 2016 1 4.2
DATE 2016 1 4.4
DATE 2016 1 4.6
DATE 2016 1 4.8
DATE 2016 1 5
DATE 2016 1 5.5
DATE 2016 1 6
DATE 2016 1 6.5
DATE 2016 1 7
DATE 2016 1 7.5
DATE 2016 1 8
DATE 2016 1 9
DATE 2016 1 10

STOP
```